Geochemistry Geophysics Geosystems G3
AN ELECTRONIC JOURNAL OF THE EARTH SCIENCES
Published by AGU and the Geochemical Society

Article
Volume 5, Number 8
18 August 2004
Q08002, doi:10.1029/2004GC000712
ISSN: 1525-2027

Hydrothermal venting in magma deserts: The ultraslow-spreading Gakkel and Southwest Indian Ridges

Edward T. Baker
NOAA Pacific Marine Environmental Laboratory, 7600 Sand Point Way NE, Seattle, Washington 98115, USA (edward.baker@noaa.gov)

Henrietta N. Edmonds
Marine Science Institute, University of Texas at Austin, 750 Channel View Drive, Port Aransas, Texas 78373, USA (edmonds@utmsi.utexas.edu)

Peter J. Michael
Department of Geosciences, University of Tulsa, 600 South College Avenue, Tulsa, Oklahoma 74104, USA (pjm@utulsa.edu)

Wolfgang Bach
Department of Marine Chemistry and Geochemistry, Woods Hole Oceanographic Institution, Woods Hole, Massachusetts 02543, USA (wbach@whoi.edu)

Henry J. B. Dick
Department of Geology and Geophysics, Woods Hole Oceanographic Institution, Woods Hole, Massachusetts 02543, USA (hdick@whoi.edu)

Jonathan E. Snow
Max-Plank-Institut für Chemie, Postfach 3060, 55020 Mainz, Germany (jesnow@mpch-mainz.mpg.de)

Sharon L. Walker
NOAA Pacific Marine Environmental Laboratory, 7600 Sand Point Way NE, Seattle, Washington 98115, USA (sharon.l.walker@noaa.gov)

Neil R. Banerjee
Department of Earth and Atmospheric Sciences, University of Alberta, 1-26 Earth Sciences Building, Edmonton, Alberta, Canada (banerjee@ualberta.ca)

Charles H. Langmuir
Department of Earth and Planetary Sciences, Harvard University, Cambridge, Massachusetts 02138, USA (langmuir@eps.harvard.edu)

[1] Detailed hydrothermal surveys over ridges with spreading rates of 50–150 mm/yr have found a linear relation between spreading rate and the spatial frequency of hydrothermal venting, but the validity of this relation at slow and ultraslow ridges is unproved. Here we compare hydrothermal plume surveys along three sections of the Gakkel Ridge (Arctic Ocean) and the Southwest Indian Ridge (SWIR) to determine if hydrothermal activity is similarly distributed among these ultraslow ridge sections and if these distributions follow the hypothesized linear trend derived from surveys along fast ridges. Along the Gakkel Ridge, most apparent vent sites occur on volcanic highs, and the extraordinarily weak vertical density gradient of the deep Arctic permits plumes to rise above the axial bathymetry. Individual plumes can thus be extensively dispersed along axis, to distances >200 km, and ~75% of the total axial length surveyed is overlain by plumes. Detailed mapping of these plumes points to only 9–10 active sites in 850 km, however, yielding a site frequency F_s, sites/100 km of ridge length, of 1.1–1.2. Plumes detected along the SWIR are

considerably less extensive for two reasons: an apparent paucity of active vent fields on volcanic highs and a normal deep-ocean density gradient that prevents extended plume rise. Along a western SWIR section (10°–23°E) we identify 3–8 sites, so F_s = 0.3–0.8; along a previously surveyed 440 km section of the eastern SWIR (58°–66°E), 6 sites yield F_s = 1.3. Plotting spreading rate (u_s) versus F_s, the ultraslow ridges and eight other ridge sections, spanning the global range of spreading rate, establish a robust linear trend (F_s = 0.98 + 0.015u_s), implying that the long-term heat supply is the first-order control on the global distribution of hydrothermal activity. Normalizing F_s to the delivery rate of basaltic magma suggests that ultraslow ridges are several times more efficient than faster-spreading ridges in supporting active vent fields. This increased efficiency could derive from some combination of three-dimensional magma focusing at volcanic centers, deep mining of heat from gabbroic intrusions and direct cooling of the upper mantle, and nonmagmatic heat supplied by exothermic serpentinization.

Components: 14,228 words, 21 figures.

Keywords: Gakkel Ridge; hydrothermal venting; magmatic budget; Southwest Indian Ridge; ultraslow ridges.

Index Terms: 3035 Marine Geology and Geophysics: Midocean ridge processes; 4832 Oceanography: Biological and Chemical: Hydrothermal systems; 8424 Volcanology: Hydrothermal systems (8135)

Received 5 February 2004; **Revised** 4 June 2004; **Accepted** 29 June 2004; **Published** 18 August 2004.

Baker, E. T., H. N. Edmonds, P. J. Michael, W. Bach, H. J. B. Dick, J. E. Snow, S. L. Walker, N. R. Banerjee, and C. H. Langmuir (2004), Hydrothermal venting in magma deserts: The ultraslow-spreading Gakkel and Southwest Indian Ridges, *Geochem. Geophys. Geosyst.*, *5*, Q08002, doi:10.1029/2004GC000712.

1. Introduction

[2] Seafloor hydrothermal discharge occurs in widely diverse geological settings along mid-ocean ridges of all spreading rates. This diversity complicates the construction of predictive models of hydrothermal activity based on geological indicators alone. One such model is the hypothesis that the spatial frequency of hydrothermal venting is a linear function of spreading rate, a proxy for the long-term magma budget [*Baker and Hammond*, 1992; *Baker et al.*, 1996]. Multi-segment-scale surveys on many ridges suggest that this relationship holds across a broad spectrum of spreading rates. Evidence to support this relationship is easily acquired along ridges with narrow, well-defined axes (i.e., ''fast spreading'' ridges), where the fraction of ridge length overlain by hydrothermal plumes is interpreted as a relative measure of the abundance of seafloor discharge [*Baker and Hammond*, 1992]. Similar surveys within the broad, deep axial valleys of ''slow-spreading'' ridges are more difficult to conduct and more problematic to interpret [*German et al.*, 1998a; *Bach et al.*, 2002], but studies along the Mid-Atlantic Ridge (MAR) do yield results that appear consistent with the trend established by faster-spreading ridges [*German and Parson*, 1998].

[3] Several recent surveys have focused on the most anomalous category of ridges, those that spread at ultraslow speeds of <20 mm/yr (full rate) [*Dick et al.*, 2003]. At such low spreading rates, decreased mantle melting may dramatically reduce seafloor volcanism and the thickness of the basaltic crust. The proposed linear relationship between spreading rate and hydrothermal activity implies that plume incidence should be lowest at ultraslow speeds [*Baker et al.*, 1996], especially considering that the magma budget at such ridges decreases more abruptly than does the spreading rate [*Reid and Jackson*, 1981; *White et al.*, 2001]. This simple view was first challenged by two recent surveys along the ultraslow Southwest Indian Ridge (SWIR). While each found a low incidence of hydrothermal plumes, in both cases that incidence appeared to be higher than expected for spreading rates of 8–15 mm/yr [*German et al.*, 1998a; *Bach et al.*, 2002].

[4] The Arctic Mid-Ocean Ridge Expedition (AMORE) in 2001 [*Edmonds et al.*, 2003; *Michael et al.*, 2003; *Jokat et al.*, 2003] provided an opportunity to map the hydrothermal plumes of an ultraslow ridge in more detail than ever before. Here we compare the detailed plume distribution along the Gakkel Ridge (Figure 1) with that along two previously surveyed sections of the SWIR (Figure 2) (including new data reported here)

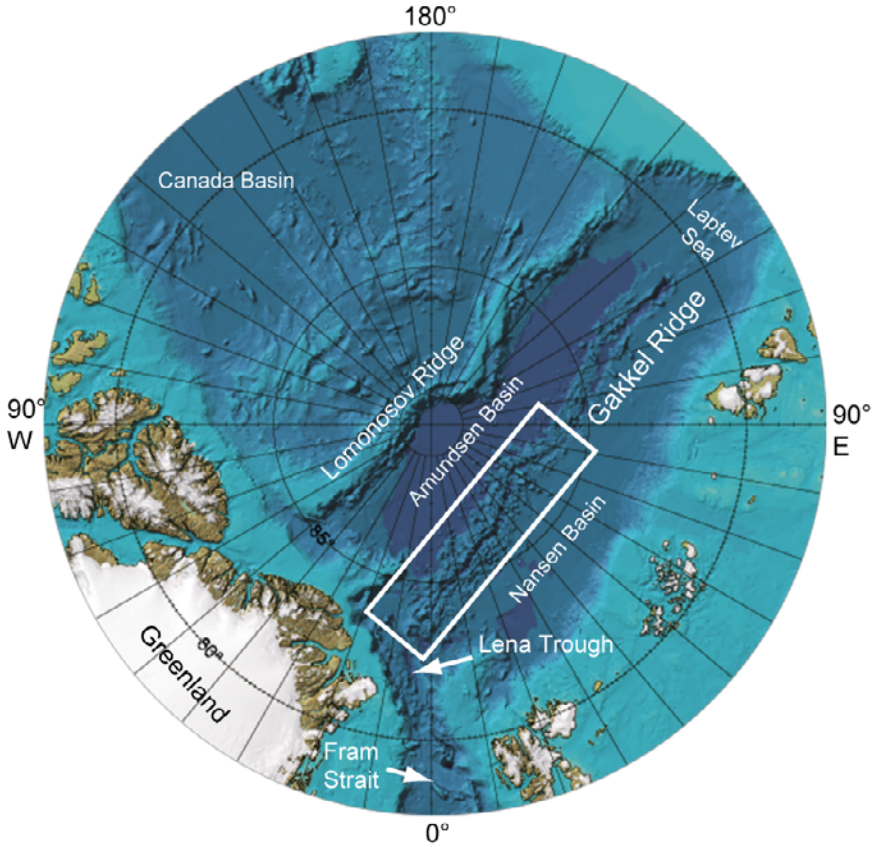

Figure 1. Location map derived from the International Bathymetric Chart of the Arctic Ocean. The white rectangle indicates the portion of the Gakkel Ridge surveyed by the AMORE project. For detailed bathymetry, see *Michael et al.* [2003].

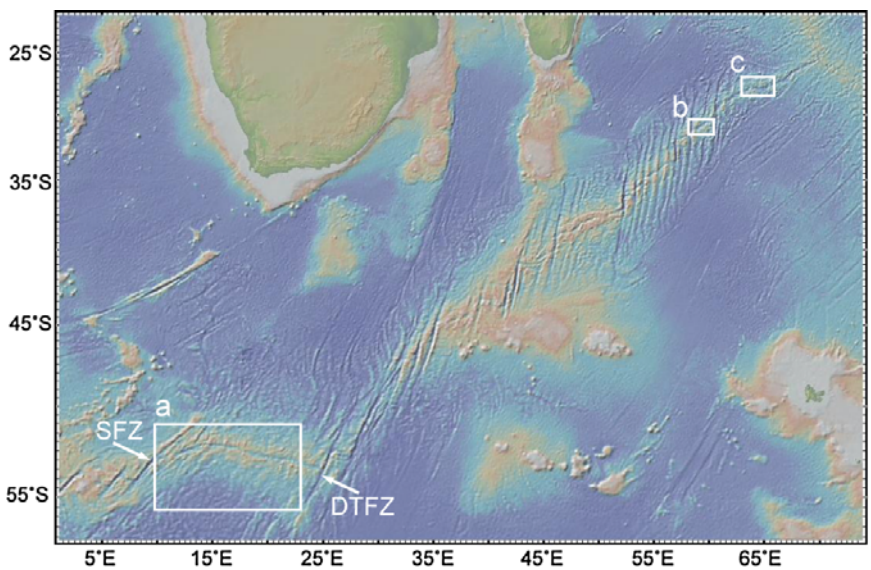

Figure 2. Location map for Southwest Indian Ridge sites. (a) Western SWIR, 10°–23°E. For detailed bathymetry, see *Grindlay et al.* [1998] and *Dick et al.* [2003]. SFZ, Shaka Fracture Zone; DTFZ, Du Toit Fracture Zone. (b and c) Two portions of the eastern SWIR, 58°30′–60°30′E and 63°30′–66°E. For detailed bathymetry, see *German et al.* [1998a].

[*German et al.*, 1998a; *Bach et al.*, 2002] to determine if the level of hydrothermal activity is similar among these ultraslow-spreading ridges and if these ridges follow the hypothesized linear global trend between hydrothermal activity and spreading rate.

2. Methods

[5] Light backscattering and temperature profiles were collected in each study area using Miniature Autonomous Plume Recorders [*Baker and Milburn*, 1997]. On the Gakkel Ridge, MAPRs were deployed on dredges (Dxx), rock cores (RCxx), and conductivity-temperature-depth instruments (CTDx) from the USCGC *Healy* and on camera lowerings (Pxxx) from PFS *Polarstern* [*Snow et al.*, 2002; *Edmonds et al.*, 2003; *Michael et al.*, 2003]. A total of 145 profiles were accumulated along 850 km of surveyed ridge (two sections of ridge were unsampled), a mean spacing of 6.6 km, although the profiles were not evenly distributed. MAPRs were typically clamped on the wire at 175 m above the dredge, 50 m above the rock core, or 30 m above the CTD rosette. Each MAPR deployment recorded both an up and down profile, which in the case of dredges and camera lowerings could be separated by as much as 2 km. MAPRs recorded light backscattering, temperature, and pressure every 5 s, or about every 8 m at the nominal dredge/rock core lowering speed of 100 m/min. Raw voltage readings from the Seapoint light backscattering sensors on the four MAPRs used by *Healy* and three used by *Polarstern* are directly equivalent to Nephelometric Turbidity Units [*American Public Health Association*, 1985]. We calculated anomalous NTU values, or ΔNTU, by filtering the raw data to remove isolated spikes caused by large particles in the water column and then subtracting the local background NTU value. ΔNTU anomalies identify hydrothermal plumes and resuspended sediments.

[6] The same instruments were used for data collection along the SWIR. *Bach et al.* [2002] presented results from 41 MAPR profiles from dredge hauls (Dxx) collected along the western SWIR from 10° to 16°E in 2000/2001 on R/V *Knorr* cruise 162. Here we discuss results from the remaining 21 profiles (17°30′–23°E) collected during that cruise plus an additional 25 profiles from a 2003 cruise on R/V *Melville*. The mean profile spacing for the combined data set is 10.9 km, almost twice that of the Gakkel Ridge data. *German et al.* [1998a] described an alternate data collection strategy along the eastern SWIR. MAPRs were affixed to the tow cable of a deep-tow side scan package that made two parallel tracks (offset by 5–6 km) through the axial valley of two neighboring ridge sections. The MAPRs swept through a 300-m-thick layer, roughly following the bathymetry, recording data every 15 m at the nominal tow speed of 1 m/s.

[7] MAPRs record temperature using an YSI 46006 thermistor (0.001°C resolution, 2.5 s maximum time constant) mounted in an external titanium probe. During the AMORE cruise we evaluated MAPR temperature data by mounting a MAPR on each of the six Sea Bird 911plus CTD casts collected. MAPRs were consistently within ~0.006°C of the CTD temperatures throughout the water column. MAPRs do not measure conductivity, so we cannot directly calculate potential temperature (θ) from the measured in situ temperatures. Instead, we produced a synthetic salinity profile by averaging all six CTD casts, using this profile to calculate θ on all MAPR casts. Below 2000 m, variability in salinity values among all casts at any depth was <0.005, too small to introduce significant error in calculating θ.

[8] The hydrothermal origin of ΔNTU can be confirmed by calculating a hydrothermal temperature anomaly (Δθ) at each depth z from an expression such as

$$\Delta\theta(z) = \theta - \left(k_n\sigma_2(z)^n + k_{n+1}\sigma_2(z)^{n+1} + \ldots + b\right), \quad (1)$$

where $\theta(z)$ is potential temperature; $\sigma_2(z)$ is potential density referenced to 2000 m; and k and b are regression coefficients for an n-order fit of θ as a function of σ_θ immediately above and below a neutrally buoyant plume. This technique is only possible for the six CTD profiles collected on the Gakkel Ridge, where we have the simultaneous θ and conductivity data required to calculate σ_2. For MAPR casts, we use an alternative procedure based on the observation that θ-z profiles unaffected by hydrothermal input are generally well described by a simple polynomial function at depths >~2000 m. Deviations from this function represent Δθ anomalies [*Lavelle et al.*, 1998], and closely match the Δθ values calculated on the six CTD casts using equation (1) (Figure 3). This technique is not practical with the SWIR data because of the absence of CTD casts and the far more complex hydrography there (compare Figures 4a and 5a).

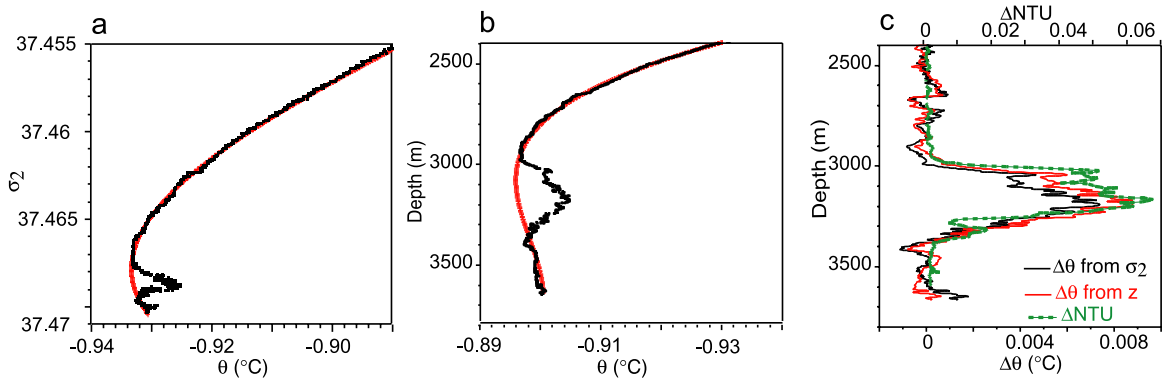

Figure 3. Calculation of the hydrothermal temperature anomaly, $\Delta\theta$, at CTD8 on the Gakkel Ridge, from (a) deviation of the θ-σ_2 relation (black line) from the background trend (red line) and (b) deviation of the θ-depth relation (black line) from the background trend (red line). In each case the background trend is a third-order polynomial fit to the profile above and below the plume layer. (c) Comparison of each calculation with the ΔNTU profile on CTD8 shows good agreement between both methods and with the optical plume signature (green dashed line).

[9] All hydrothermal plumes identified in this paper originate at vents that are almost certainly hosted at least in part by basaltic/gabbroic rock. Hydrothermal fields powered solely by serpentinization, typified by the Lost City Field on the MAR [*Kelley et al.*, 2001] and expected to be common on ultraslow ridges, discharge low-temperature fluids nearly devoid of suspended hydrothermal precipitates. These characteristics make their plumes weak and effectively invisible to optical and hydrographic sensors. If hydrothermal discharge at ultraslow ridges is dominantly by low-temperature fluids without accompanying flow that produces detectable optical anomalies, then we will seriously under-estimate the venting frequency. Only detailed seafloor investigations can address this issue.

3. Physical Setting of the Gakkel and Southwest Indian Ridges

3.1. Geological Setting

[10] *Dick et al.* [2003] have recently identified ultraslow-spreading ridges as a new class that is tectonically, magmatically, and hydrothermally distinct from other ridges. Important characteristics of this ridge class, which includes the Gakkel Ridge and long stretches of the SWIR, include an absence of transform faults, rift valley walls defined by extremely long-lived low-angle faults, and long stretches of seafloor where mantle peridotite is emplaced directly to the seafloor with little or no volcanic cover between widely spaced isolated magmatic centers.

[11] The geology and geophysics of the Gakkel Ridge have been summarized in several recent papers [*Cochran et al.*, 2003; *Michael et al.*, 2003; *Jokat et al.*, 2003; *Dick et al.*, 2003]. The entire ridge traverses some 1800 km from the Lena Trough, northeast of Greenland, eastward to the Laptev Sea (Figure 1). The AMORE project collected MAPR profiles from 6°30′W to 85°E, a ridge length over which spreading rates decline from 14 to 11 mm/yr. Axial valley depths can exceed 5000 m and valley widths (at the top of the bounding walls) range from 10 to >30 km. Except near the large volcanic edifices, axial valley relief along most of the ridge is ~1500–2000 m (Figure 4) [*Cochran et al.*, 2003; *Brozena et al.*, 2003] (AMORE bathymetry generally did not reach to the summits of the valley walls). East of ~43°E, flank topography becomes subdued and deeper, and east of 69°E several hundred meters of sediments almost bury the rift valley.

[12] *Michael et al.* [2003] divide the study area into three magmato-tectonic domains: a Western Volcanic Zone, a central Sparsely Magmatic Zone, and an Eastern Volcanic Zone (Figure 4a). The Western Volcanic Zone (7°W–3°E) contains evidence of abundant volcanism, including large volcanic ridges at 1°30′ and 4°30′W and numerous smaller ridges and cones evocative of the faster spreading northern MAR. The Sparsely Magmatic Zone (3°–29°E), separated from the Western Volcanic Zone by a 10-km offset, is ~1 km deeper than the Western Volcanic Zone and contains only isolated volcanic centers at 13° and 19°E. Spreading in this section appears to be largely amagmatic, with peridotite exposures common on the seafloor.

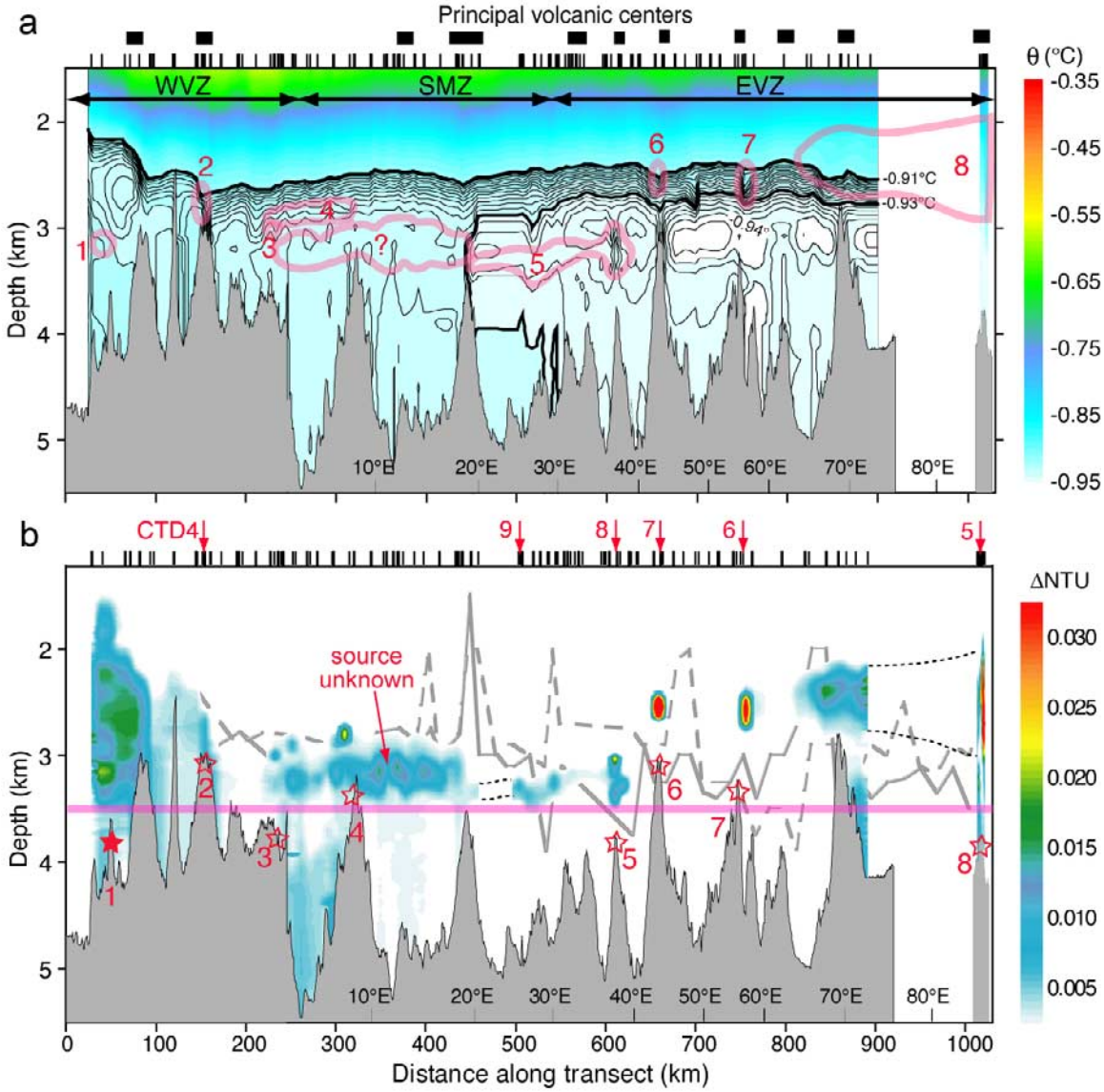

Figure 4. (a) Along-axis transect of θ over the Gakkel Ridge. Black bars above the panel show locations of the principal volcanic centers; extent of the magmato-tectonic zones (WVZ, Western Volcanic Zone; SMZ, Sparsely Magmatic Zone; EVZ, Eastern Volcanic Zone) is shown by double-headed arrows [*Michael et al.*, 2003]. Locations of the 111 profiles used here (many of the 145 total are redundant at this scale) are given by ticks along the top of the panel. Contours at 0.002°C intervals shown for $\theta \leq -0.91$°C. Plume outlines from Figure 4b are superimposed to illustrate the control of plume geometry by the temperature (density) field. (b) Along-axis transect of ΔNTU. Red arrows show CTD locations. Red stars show proposed active sites, filled where confirmed by seafloor imagery. Dashed lines connecting plume layers suggest continuity in two broad sections with no profile data. Gray lines give maximum heights of the north (dashed) and south (solid) flanking valley walls at 2° intervals from bathymetry between 10°E and 70°E [*Cochran et al.*, 2003] and interpolated from gravity data [*Brozena et al.*, 2003] elsewhere. The pink horizontal line marks the top of the bottom isopycnal layer, above which all plumes rise. Some weak plume signatures are apparent on individual profiles but not in this gridded data (e.g., within the westward trending plume from site 4).

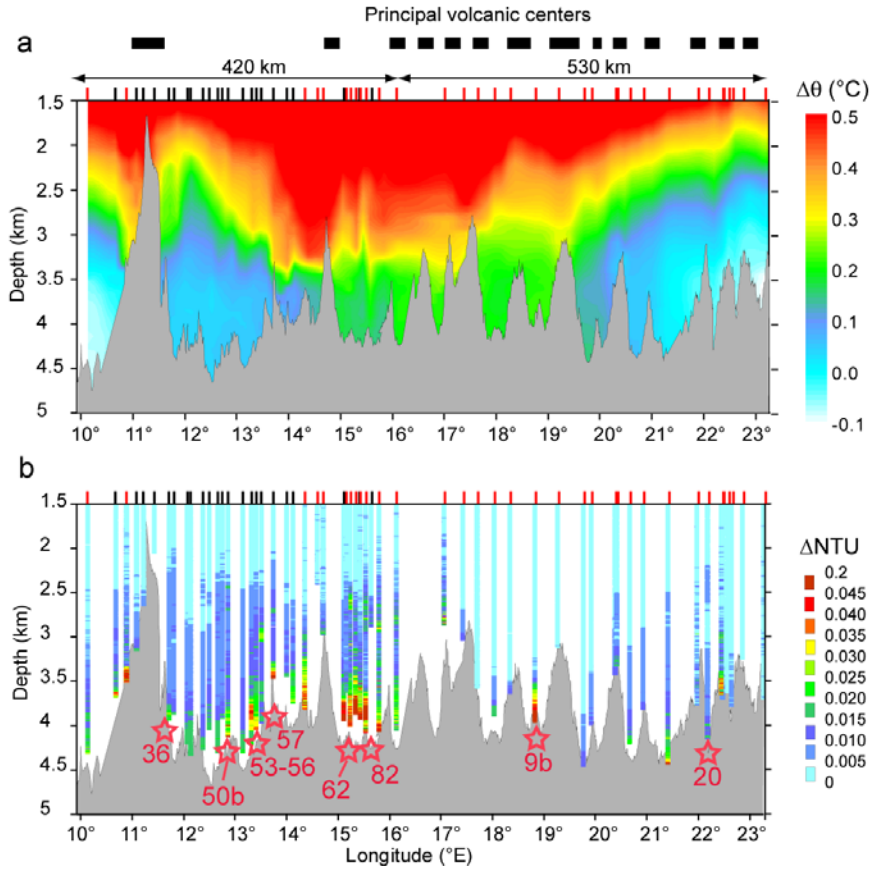

Figure 5. (a) Along-axis transect of θ on the western SWIR, using new data (red ticks on panel top) and profiles reported by *Bach et al.* [2002] (black ticks). The black bars at the top show locations of the principal volcanic centers [*Grindlay et al.*, 1998; *Dick et al.*, 2003]. (b) Along-axis transect of ΔNTU from the same profiles. Unlike in Figure 5a, these data are not contoured because gridding would obscure the near-bottom variability. Location of inferred hydrothermal plume signals indicated by red stars labeled with corresponding dredge numbers. Compare the temperature field here with that along the Gakkel Ridge, noting that the θ range is the same in each figure.

The Eastern Volcanic Zone (29°–85°E) remains deep but is punctuated by at least six large volcanic centers (31°E, 37°E, 43°E, 55°E, 69°E, 85°E). Basalt was ubiquitous in Eastern Volcanic Zone dredges, and was especially fresh at 85°E where side scan images [*Edwards et al.*, 2001] and a 1999 earthquake swarm [*Muller and Jokat*, 2000; *Tolstoy et al.*, 2001] strongly indicate recent volcanic eruptions.

[13] Hydrothermal plumes have been mapped along three sections of the SWIR, one at the western end and two near the eastern end (Figure 2). The western section (Figure 5) extends from 10° to 25°E and contains two major segments: an eastern orthogonal supersegment (16°–25°E) opening at ~15 mm/yr [*Grindlay et al.*, 1998; *Dick et al.*, 2003] and a western supersegment (10°–16°E) highly oblique to the regional spreading direction with an effective (perpendicular to the ridge trend) spreading rate for mantle upwelling of only 7.8–12.4 mm/yr [*Dick et al.*, 2002, 2003; *Bach et al.*, 2002]. The orthogonal supersegment is punctuated by numerous volcanic centers with relief of ~1000 m, while the oblique supersegment is deeper and largely magma starved, with only two major volcanic centers (Figure 5), similar to the Sparsely Magmatic Zone on the Gakkel Ridge. Crustal thickness of the oblique supersegment is <1 km [*Dick et al.*, 2003].

[14] At the far eastern end of the SWIR, *German et al.* [1998a] mapped hydrothermal plumes along two contrasting sections on either side of the Melville Fracture Zone (Figures 2 and 6a). The regional full spreading rate here is 16 mm/yr, but the oblique orientation of the 58°30′E–60°E section reduces the net rate to 14 mm/yr. The

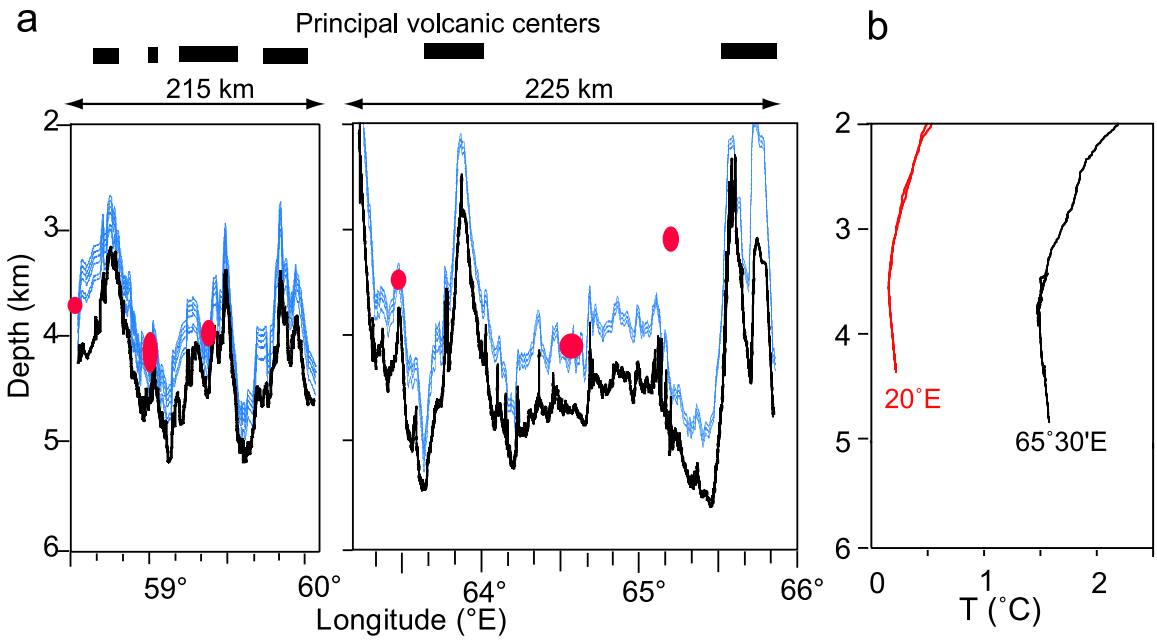

Figure 6. (a) Bathymetry (heavy black line) and MAPR tow paths (light blue lines) along two sections of the eastern SWIR. The black bars at the top show locations of the principal volcanic centers [*Sauter et al.*, 2002; *Cannat et al.*, 2003]. Red dots indicate ΔNTU anomalies [*German et al.*, 1998a]. This diagram shows only one of two parallel tracks; the plume at 65°10′E was detected on the other track, which followed a slightly different bathymetry (see *German et al.* [1998a] for detailed bathymetry and track lines). (b) In situ temperature (not θ) profiles from the western (20°E, red line) and eastern (65°30′E, black line) SWIR. Temperature gradients are similar even though the deep water warms toward the north.

eastern section (63°30′–66°E) is magma-poor with large but infrequent volcanic constructs; the western section (58°30′–60°E) resembles MAR bathymetry, with more moderate relief and widespread volcanic features [*Cannat et al.*, 1999, 2003; *Sauter et al.*, 2002].

3.2. Oceanographic Setting

[15] The Gakkel Ridge inhabits a hydrographic regime that is unique among Earth's spreading ridges. The Arctic Ocean below ~1 km is bathymetrically isolated from the rest of the global ocean, so the hydrography of the deep waters within each major Arctic sub-basin is remarkably uniform [*Aagaard et al.*, 1985; *Anderson et al.*, 1994]. Below ~2000 m, θ contours along the Gakkel Ridge are nearly horizontal, and deviations from this pattern offer clues to the deep circulation (Figure 4a). At the western end of the ridge, for example, an upturn of the θ contours at depths <2500 m implies an intrusion of colder water from the adjacent Lena Trough [*Aagaard et al.*, 1985; *Rudels et al.*, 1999]. Below ~3000 m there is a distinct eastward cooling, including a remarkable thermal front across a bathymetric high at 19°E where θ changes by ~0.01°C over a distance of <10 km. Eastward of this front lies a persistent θ minimum between 3100 and 3500 m. Vertical casts taken in the Gakkel Ridge near 0° and 58°E in 1991 found similar east-west θ differences, including a θ minimum at 58°E, a feature observed over much of the eastern Eurasian Basin [*Anderson et al.*, 1994]. While no deep current measurements have been conducted in the central Eurasian Basin, models [*Nost and Isachsen*, 2003] and hydrographic inferences [*Jones et al.*, 1995] imply a slow (<1 cm/s) regional drift to the west, parallel to the Gakkel Ridge. (The first demonstration of this flow occurred in 1894–1896 as the ice-bound *Fram* drifted over the Gakkel Ridge [*Nansen*, 1897].) The θ minimum layer apparently denotes water deflected from the anticlockwise Arctic Circumpolar Current as it impinges upon the continental slope beneath the Laptev Sea. Below ~3500 m the axial valley is virtually isothermal, allowing hydrothermal plumes a nearly uninhibited rise to a depth above most of the along-axis bathymetric highs. Temperatures deeper than ~3500 m are colder than about −0.92°C, in agreement with

historical values for the Eurasian Basin [*Aagaard et al.*, 1985; *Anderson et al.*, 1994]. Density profiles from the six CTD casts confirm that this isothermal layer is also effectively isopycnal.

[16] The oceanographic environment of the western SWIR bears little resemblance to the Arctic Ocean. The deep water is strongly influenced by intrusions of cold Antarctic Bottom Water via the Shaka Fracture Zone on the west and the Du Toit FZ on the east (Figures 2 and 5a). As indicated by the θ field, both the vertical and horizontal density stratifications are much higher along the SWIR (Figure 5a) than along the Gakkel Ridge (Figure 4a). These hydrographic differences, compounded by a lower spatial density of profiles than along the Gakkel Ridge, make identification of hydrothermal activity on the western SWIR difficult. Plume rise above the local bathymetry is inhibited by the hydrography, and resuspended bottom sediments can mask or mimic hydrothermal plumes. We can't construct a corresponding temperature transect for the two eastern SWIR sections because the MAPRs were towed near the seafloor rather than profiled vertically, but a comparison of typical temperature profiles from the eastern and western SWIR areas indicates that the vertical temperature structure within each is similar (Figure 6b).

4. Gakkel Ridge Hydrothermal Plume Distribution

[17] Optical anomalies observed during AMORE were remarkably and unexpectedly widespread throughout the entire Gakkel Ridge, and are overwhelmingly concentrated between 2000 and 3500 m (Figure 4b). Most of the axial bathymetric highs lie below this plume layer and offer few obstructions to along-axis dispersal. Following the conclusions and nomenclature of *Edmonds et al.* [2003], we here describe in detail the settings of eight sites with convincing evidence of active venting, plus the characteristics of one prominent plume for which no source location can be pinpointed.

4.1. Site 1: "Aurora," 6°20′W

[18] West of a large volcanic ridge at 4°30′W, ΔNTU anomalies fill the axial valley from the seafloor to at least 2000 m (Figure 4b). The ΔNTU maximum between 2000 and 3000 m corresponds to a distinct cold-water parcel ($\theta < -0.9$°C), consistent with water temperatures found in Fram Strait/Lena Trough [*Aagaard et al.*, 1985; *Rudels et al.*, 1999]. This thick ΔNTU maximum may originate by erosion off the Fram Strait sill (2600 m), but could also represent sediments eroded by deep waters flowing southeast along the Greenland continental slope [*Jones et al.*, 1995]. Superimposed on this ΔNTU distribution is a distinct hydrothermal plume signature above a cross-axial bathymetric high (Figure 7). Aurora, imaged at 6°15′W, 82°53′N, by a *Polarstern* camera tow, is the only hydrothermal site visually confirmed as active during AMORE. D8 (Figure 7) also recovered abundant unweathered sulfide rocks at this site. Three profiles in the valley axis recorded prominent ΔNTU and Δθ (as high as 0.01°C) anomalies between 3000 and 3500 m, significantly more intense than the nonhydrothermal ΔNTU anomalies that extended to depths above 2000 m. By at least 30 km east of site 1 (P220 in Figure 7b), the Aurora plume had dissipated and the Lena Trough turbidity had assumed a smooth profile with a maximum centered at 2500–3000 m.

4.2. Site 2: 1°45′W

[19] East of 4°30′W stretch a series of volcanic segments, each delineated by a saddle point and an elongate axial high. The largest of these is located at 1°45′W, where nonhydrothermal ΔNTU anomalies are much weaker and rise no higher than ~2500 m (Figure 4b). D21, located in the middle of the southwest face of the 1°45′W volcanic ridge (Figure 8), recorded one of the most intense plumes of the AMORE cruise. The plume was sharply bounded between 2400 and 2700 m and showed distinct layering indicative of multiple, nearby seafloor sources. Δθ values reached ~0.02°C and were congruent with the ΔNTU profiles. Only near-bottom remnants of this plume were detected on two profiles 2–4 km to the east, and no evidence of it was apparent on profiles ~10 km distant on either end of the ridge. Between this mound and site 3 lies a straight, unimpeded valley within which no hydrothermal ΔNTU anomalies are detectable.

4.3. Site 3: 2°10′E

[20] Six MAPR stations were occupied between 2° and 3°E at the eastern end of the Western Volcanic Zone, mostly around the perimeter of an axial depression bounded on the northeast by a ~4000-m-deep bathymetric sill that marks the western boundary of the Sparsely Magmatic Zone (Figure 9). These profiles intercept three separate

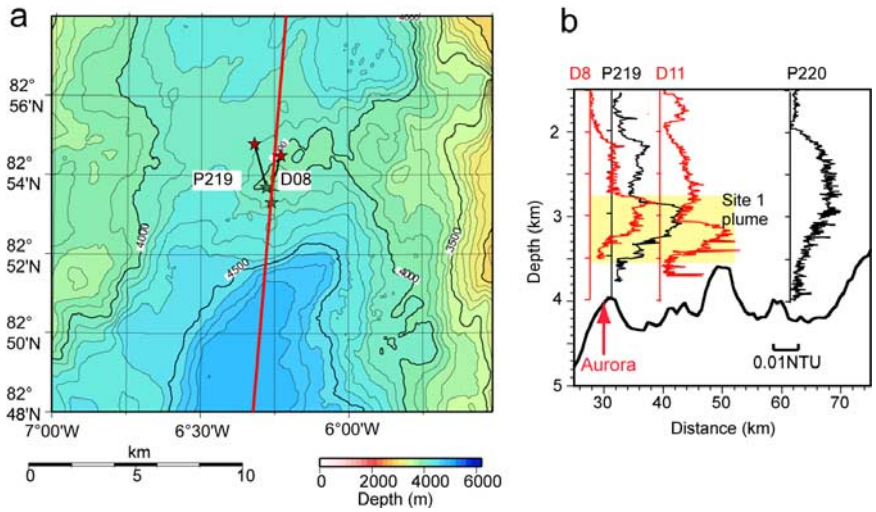

Figure 7. (a) Location map and (b) plume ΔNTU profiles from the site 1 region, where the Aurora vent field was discovered. Fresh sulfide rocks were recovered in D8. Some of the profiles are colored for clarity. Green stars on the map show the ship location at the start of an operation, and red stars show the location at the end. Bathymetry cross section follows the red line on the map. The scale bar on the profile panel equals 0.01 NTU, and vertical lines give the station location in terms of total along-axis distance from the western boundary of the AMORE bathymetry (82°35′N, 6°30′W). Station depths may not match depths on the bathymetry cross section, especially when the stations were located off the cross-section path. The pale yellow band highlights the hydrothermal plume layer. Note that the distance in Figure 7b extends beyond the map boundaries in Figure 7a. The location map has a grid cell size of 50 m and a general stereographic projection.

plume layers. The deepest and thickest layer marks the western limit of a plume that extends from 2° to 19°E (Figure 4). All but the westernmost profile show evidence of a weaker, thinner plume at ~2900 m that we suspect is a remnant of the especially intense plume from site 4, some 90 km to the east. Between these layers, however, and observed on the downcast but not the upcast of D5,

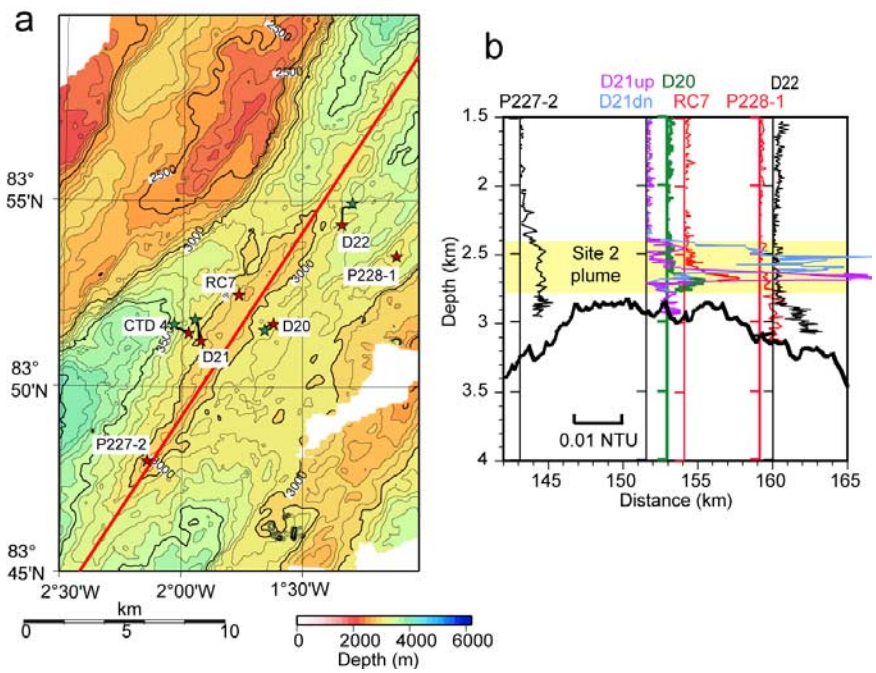

Figure 8. (a) Location map and (b) plume ΔNTU profiles from the site 2 region. Symbols, map characteristics, and legend are as in Figure 7. Note the difference in the up (purple) and down (blue) profiles at D21.

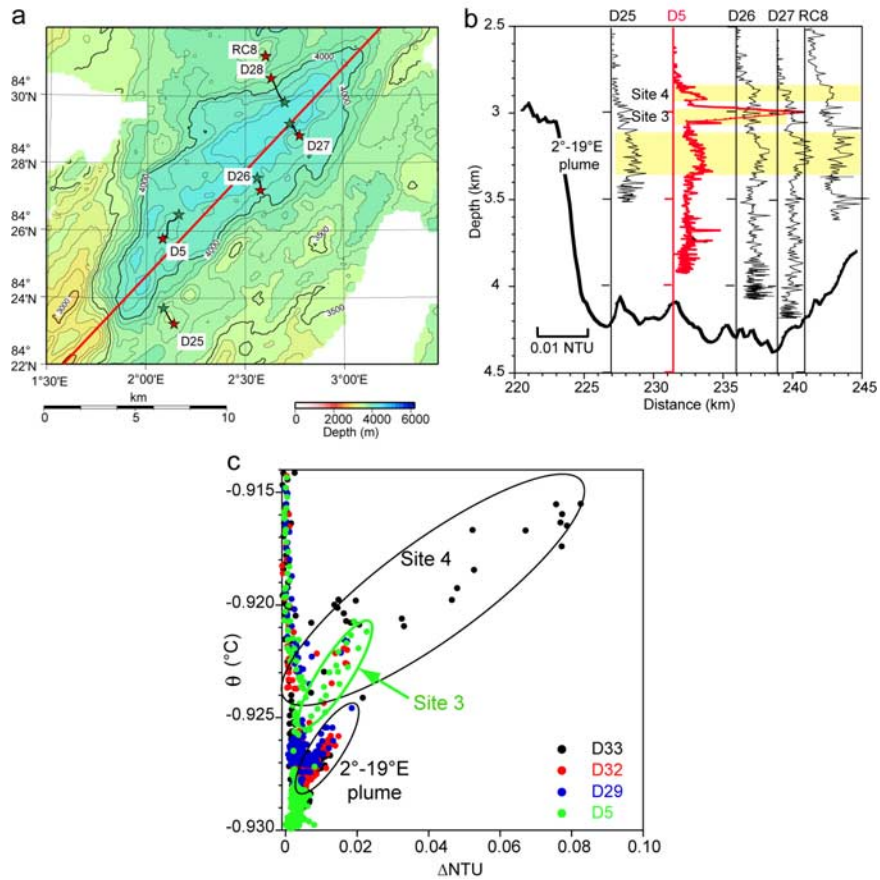

Figure 9. (a) Location map and (b) plume ΔNTU profiles from the site 3 region. Symbols, map characteristics, and legend are as in Figure 7. Some profiles are colored for clarity. (c) Scatterplot showing distinct ΔNTU versus θ trends for plumes from Site 3, Site 4, and the 2°–19°E plume.

was a thin, high vertical gradient plume with clear anomalies in both particles (0.025 ΔNTU) and temperature (0.006°C Δθ). Both the plume shape (indicating a plume not yet smoothed by vertical mixing) and the absence of any other plumes at this depth support a nearby origin. *Edmonds et al.* [2003] postulated a source on the steep valley walls to the west; another possibility is one of the volcanic cones and ridges that rise to at least 3500 m along the valley axis. The lack of a corresponding plume on the adjacent profiles may be related to timing: D5 was conducted 10 days earlier than any of the other operations in this area.

[21] We can also distinguish these three plume layers on the basis of differing θ/ΔNTU ratios (Figure 9c). This ratio is formed by mixing between the discharged fluids and the ambient seawater at the plume source. Once the plume reaches a level of neutral buoyancy and begins to spread laterally, the ratio can only change by mixing with water of a different θ/ΔNTU ratio or by a change in NTU due to particle settling, dissolution, or precipitation. These possibilities seem unimportant here because the θ/ΔNTU ratio for each plume layer in Figure 9c remains constant as the plume dilutes. The θ/ΔNTU values for the 3000-m-depth plume over site 3 (D5), for example, partially overlap the site 4 values, but appear to represent an independent population (Figure 9c).

4.4. Site 4: 7°30′E

[22] The only identified site located within the ~280-km-long Sparsely Magmatic Zone occurs on an elongate axial ridge centered near 7°30′E in the most peridotite-rich section of the Gakkel Ridge, where dredging found no evidence of volcanic activity [*Michael et al.*, 2003]. An extensive suite of partially serpentinized peridotites were recovered in D34, demonstrating that the south-facing wall of the ridge is a low-angle fault surface on which a mantle block was emplaced to form the

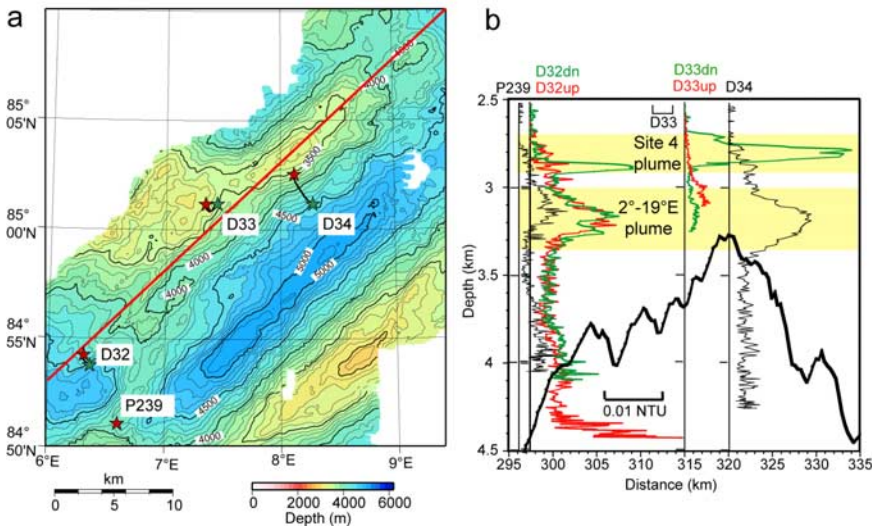

Figure 10. (a) Location map and (b) plume ΔNTU profiles from the site 4 region. Symbols, map characteristics, and legend are as in Figure 7. Note the separate 0.01 NTU scale bar for D33. The site 4 plume is laterally discontinuous but can be tracked as far west as 2°E (see Figure 9).

rift valley wall. Similar ridges make up rift valley walls on amagmatic portions of the SWIR [*Dick et al.*, 2003], and likely have a common origin. D34 included numerous carbonate-serpentine concretions cemented by radiating carbonate needles indicative of at least local low-temperature hydrothermal flow along this fault.

[23] At the top of the ridge's south-facing wall, the downcast of D33 (empty dredge) recorded an intense, layered plume between 2700 and 2900 m with ΔNTU > 0.08 and Δθ > 0.008°C (Figure 10). The D33 upcast, <1 km west, remarkably showed no evidence of this plume. The high spatial variability of this plume, combined with the steep vertical gradients of particles and heat at its boundaries, indicates a nearby source, perhaps at the base of the wall. While the gridded data (Figure 4b) gives the impression that this plume is localized to the vicinity of the D33 location, examination of individual profiles reveals a persistent ΔNTU anomaly centered around 2900 m extending as far west as 2°10′E (~85 km) (Figure 9). This depth is slightly deeper than the center of the plume at site 4, but a scatterplot of ΔNTU versus θ values for selected stations between D33 and D5 shows that the θ/ΔNTU ratio within this plume is approximately constant over the entire 85 km distance (Figure 9c). The highest θ and ΔNTU values are found closest to the presumed seafloor source (D33), and subsequent plume dilution maintains a steady θ/ΔNTU ratio within the plume. This scatterplot also shows a constant, but distinctly different, θ/ΔNTU ratio for the deeper (3100–3400 m), thicker 2°–19°E plume.

4.5. The 2°–19°E Plume Layer

[24] Overlaying sites 3 and 4, a plume layer between 3100 and 3400 m extends unbroken from 2°E, just west of the 10 km offset that separates the Western Volcanic and the Sparsely Magmatic Zones, to the thermal front overlying the prominent volcanic edifice at 19°E, some 200 km distant (Figure 11). Intensity at the plume maximum fluctuates from <0.005 to >0.015 ΔNTU, being higher in the middle and weaker at either end (Figure 4b). The top of the plume layer parallels the sloping −0.928°C isotherm (Figure 4a), and the θ/ΔNTU values within the plume are uniform and distinct from those in the site 3 or 4 plumes (Figure 9c). While we can identify no specific source location for this plume, it almost certainly lies in the Sparsely Magmatic Zone. Analogous nonvolcanic hydrothermal settings have been found on the wall of the central amagmatic trough of the SWIR oblique supersegment (10°–16°E) [*Bach et al.*, 2002]. Fossil hydrothermal deposits dredged there evidently represent discharge localized by the deep, long-lived faults on which the ultramafic massifs were emplaced into the rift valley and subsequently up onto the rift valley walls.

4.6. Site 5: 37°E

[25] The next unambiguous hydrothermal site is some 300 km farther east, well into the Eastern

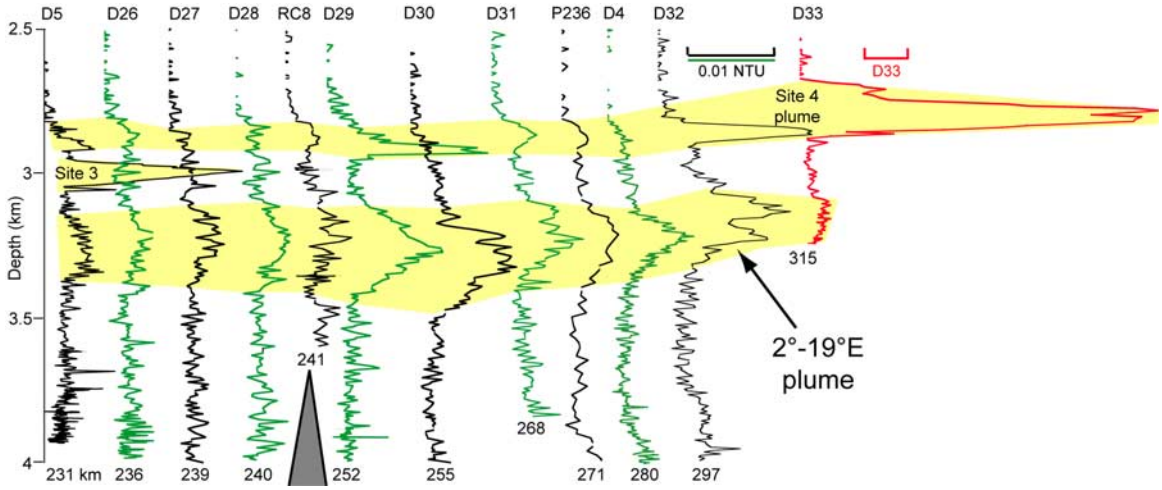

Figure 11. Plume ΔNTU profiles for stations between 2°10′E (D5) and 7°25′E (D33). Symbols, map characteristics, and legend are as in Figure 7; colors alternate for clarity. Note the separate 0.01 NTU scale bar for D33. The axial offset separating the Western Volcanic Zone from the Sparsely Magmatic Zone occurs near RC8, at 241 km from the western end of the survey. The upper two plumes originate at site 3 (Figure 9) and site 4 (Figure 10). The lower plume is persistent over this ridge length and extends eastward to 19°E, but no source site can be confidently identified.

Volcanic Zone, coinciding with the location of an elongate volcanic ridge at 37°E where D50 recovered fresh to lightly weathered glassy pillow basalt. Three stations along the crest of this ridge recorded intense and highly variable plume layers between 3000 and 3500 m (Figure 12). The largest anomalies were comparable to those at D33 (>0.065 ΔNTU and >0.008°C Δθ), and the distinct difference in plume layering between the up- and downcasts of D50 suggests a nearby vent field with multiple vigorous sources. Six other stations in the vicinity all showed weak but distinct plumes within the same depth range (Figure 12), supporting the inference that the seafloor source is on the ridge, most likely close to CTD8 or D50. We further suggest that this site is the origin of the extensive 19°–42°E plume, whose plume maximum slowly rises from 3400 m at 19°E to 3200 m at 37°E, exactly following the core of the θ minimum layer east of 19°E (Figure 4a). The plume ends abruptly on the western slope of the 43°E volcanic edifice, even though there is a narrow sill which sinks to 3800–3900 m on its north side. A scatterplot of ΔNTU versus θ for four stations between 19° and 42°E shows that dilution of the site 5 plume leads directly to the θ/ΔNTU characteristics of the entire extensive plume (Figure 12c). Temperatures within the site 5 plume are ~0.01°C cooler than in the site 4 plume (Figures 9 and 12c).

4.7. Site 6: 43°10′E

[26] Site 6 is likely located near the summit of the 43°E volcanic ridge on the south side of the axial valley (Figure 13). Light to moderately weathered pillow basalt was recovered in D51 and D52 on the NW flank of the volcano, while fresh glassy pillow basalt was recovered in D83 along the ridge crest. Of the 6 stations on the ridge, RC18 and CTD7 both recorded a substantial multilayered plume, with ΔNTU > 0.1 and Δθ > 0.01°C. Stations even a few km east and west found only a feeble plume at the same depth interval (2400–2700 m). Unlike plumes to the west, those from sites 6, 7, and 8 all rise hundreds of meters above the valley walls (Figure 4b). We surmise that the combination of a relatively shallow vent field and locally deep flanking walls allows the site 6 plume to be dispersed away from the ridge rather than trapped and transported along the axial valley.

4.8. Site 7: 55°20′E

[27] The setting and plume characteristics of site 7 effectively duplicate those of site 6. Dredging up the base of the north-facing wall of an axial volcanic mound near 56°E recovered only light to moderately weathered pillow basalt. Of 5 stations around this ridge, only D74 detected a concentrated plume. Multiple layers, high vertical gradients, and concentrated anomalies suggest that D74 was near the plume source even though nearby profiles found only weak anomalies in the 2400–2700 m depth interval (Figure 14). As at site 6, the plume rises above the surrounding flank walls and is not trapped within the axial valley. Very faint evidence (ΔNTU ~0.002) of both the site 6 and 7 plumes was detectable only within 10–

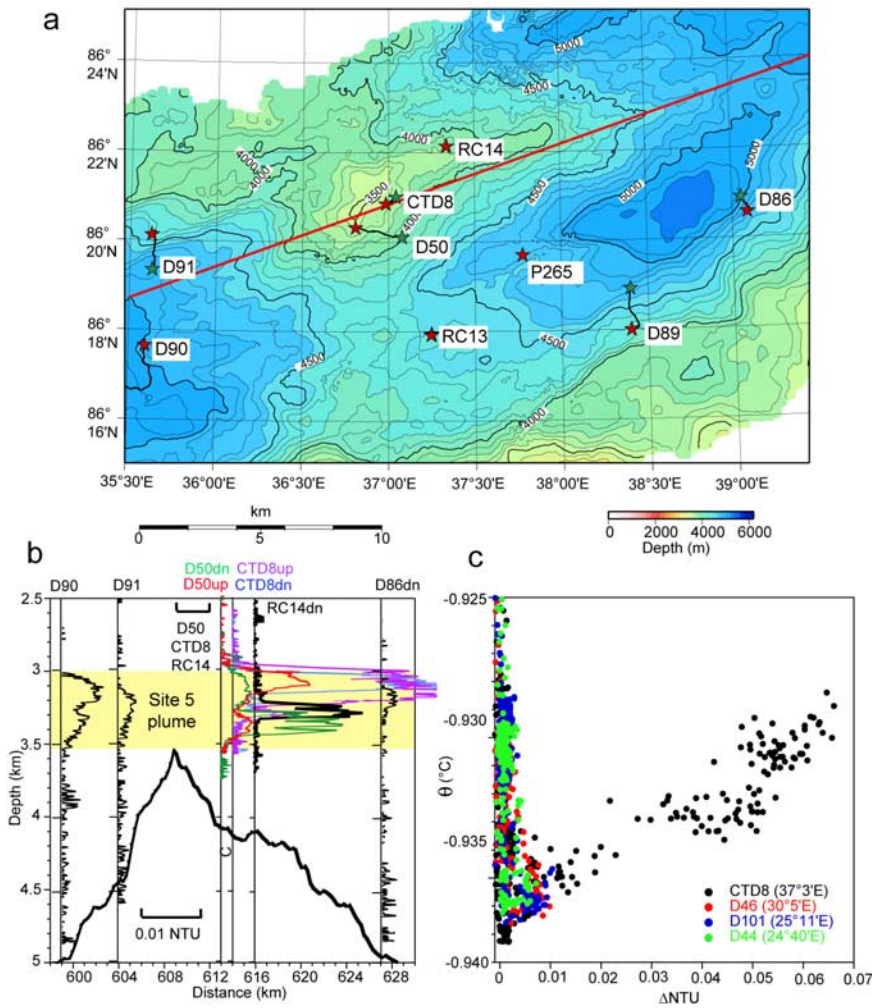

Figure 12. (a) Location map and (b) plume ΔNTU profiles from the site 5 region. Symbols, map characteristics, and legend are as in Figure 7. Note the separate 0.01 NTU scale bar for D50, CTD8, and RC14. (c) Scatterplot showing that dilution of the near-source site 5 plume (CTD8) maintains a constant θ/ΔNTU ratio as least as far west as 24°40′E.

30 km from the presumed sources, so plume dilution at these sites was far more effective than at sites to the west.

4.9. Site 8: 85°E

[28] Our interpretation of hydrothermal sites at the eastern end of the study area is complicated by a 120 km gap in plume coverage from 73°E to 84°E, the result of deteriorating ice conditions that precluded sampling. A volcanic edifice stretching from 66°E to 73°E and centered at 69°E is the most prominent landmark here (Figure 15). Several dredges along this volcanic ridge recovered light to moderately weathered, often very glassy sheet flows and pillow basalts, with fresh glassy basalt recovered in D67. At the eastern limit of the study area, a cluster of volcanic cones near 85°E yielded light to moderately weathered, very glassy pillow basalts in D61, D63 and D64, while fresh glassy pillow basalts were recovered in D62.

[29] From about 58° to 65°E, where the ridge axis turns about 40° abruptly to the southeast, vertical profiles begin to intersect a broad plume layer between ~2200 and 2900 m (too faint to be resolvable on Figure 4). At 67°30′E (RC17) the plume intensity swells several-fold and shows clear layering in both ΔNTU and Δθ over the next 50 km of ridge crest length (Figure 15). *Edmonds et al.* [2003] viewed these plumes in the same light as those over the volcanic centers at 43° and 55°E, postulating an active hydrothermal site somewhere near the large volcanic edifice stretching from 66°E

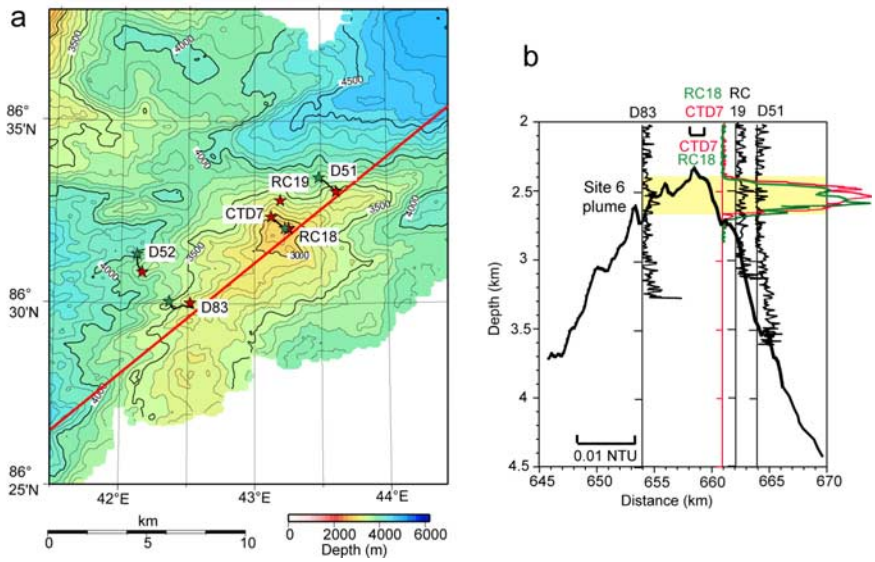

Figure 13. (a) Location map and (b) plume ΔNTU profiles from the site 6 region. Symbols, map characteristics, and legend are as in Figure 7. Note the separate 0.01 NTU scale bar for CTD7 and RC18.

to 73°E and centered at 69°E. Unlike other sites, however, no profile stands out as closer to a source than any other, and ΔNTU maxima never exceed ~0.02, smaller than every site except 1 and 3. (The near-bottom ΔNTU anomalies east of 69°E have no corresponding Δθ signature and presumably originate by resuspension of the thick sedimentary layer that blankets the axial valley from ~70°E to at least 98°E [*Cochran et al.*, 2003].)

[30] Since we cannot confidently identify a local plume source near the 69°E volcano, we propose that the 50-km-long plume over the 69°E volcano in fact originates near 85°E, site of the most vigorous discharge encountered along the Gakkel Ridge. The 85°E site (site 9 of *Edmonds et al.* [2003]) was densely sampled with eight stations around a volcanic mound rising a few hundred meters above the 4000-m-deep valley floor (Figure 15), and a ninth station on the flank of a nearby volcano summiting at ~2500 m. Near the center of the axial mound (D61), a vertically symmetrical plume extends from 1700 to 3100 m, with ΔNTU > 0.09 and Δθ > 0.07°C, by far the largest Δθ value recorded on the Gakkel Ridge. Outward from D61, both along and across valley, the plume thins and exhibits distinct layering, with clear evidence of deeper plumes at several stations (e.g., D64). These profiles compellingly support the evidence from teleseismic recordings [*Muller and Jokat*, 2000; *Tolstoy et al.*, 2001] and side scan images [*Edwards et al.*, 2001] that a massive and

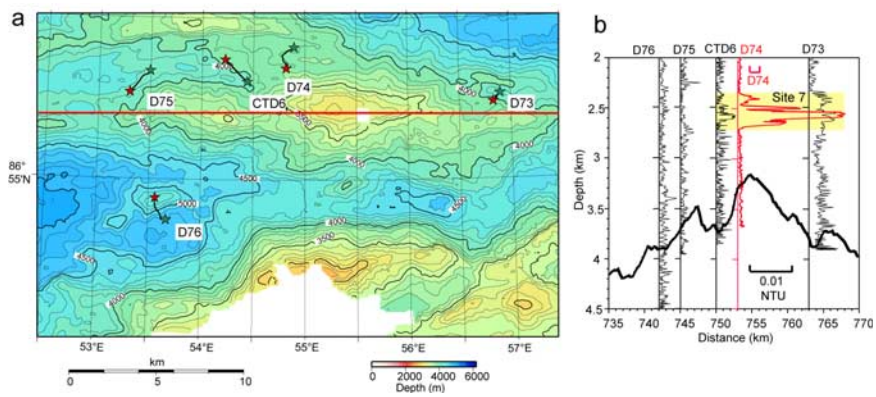

Figure 14. (a) Location map and (b) plume ΔNTU profiles from the site 7 region. Symbols, map characteristics, and legend are as in Figure 7. Note the separate 0.01 NTU scale bar for D74.

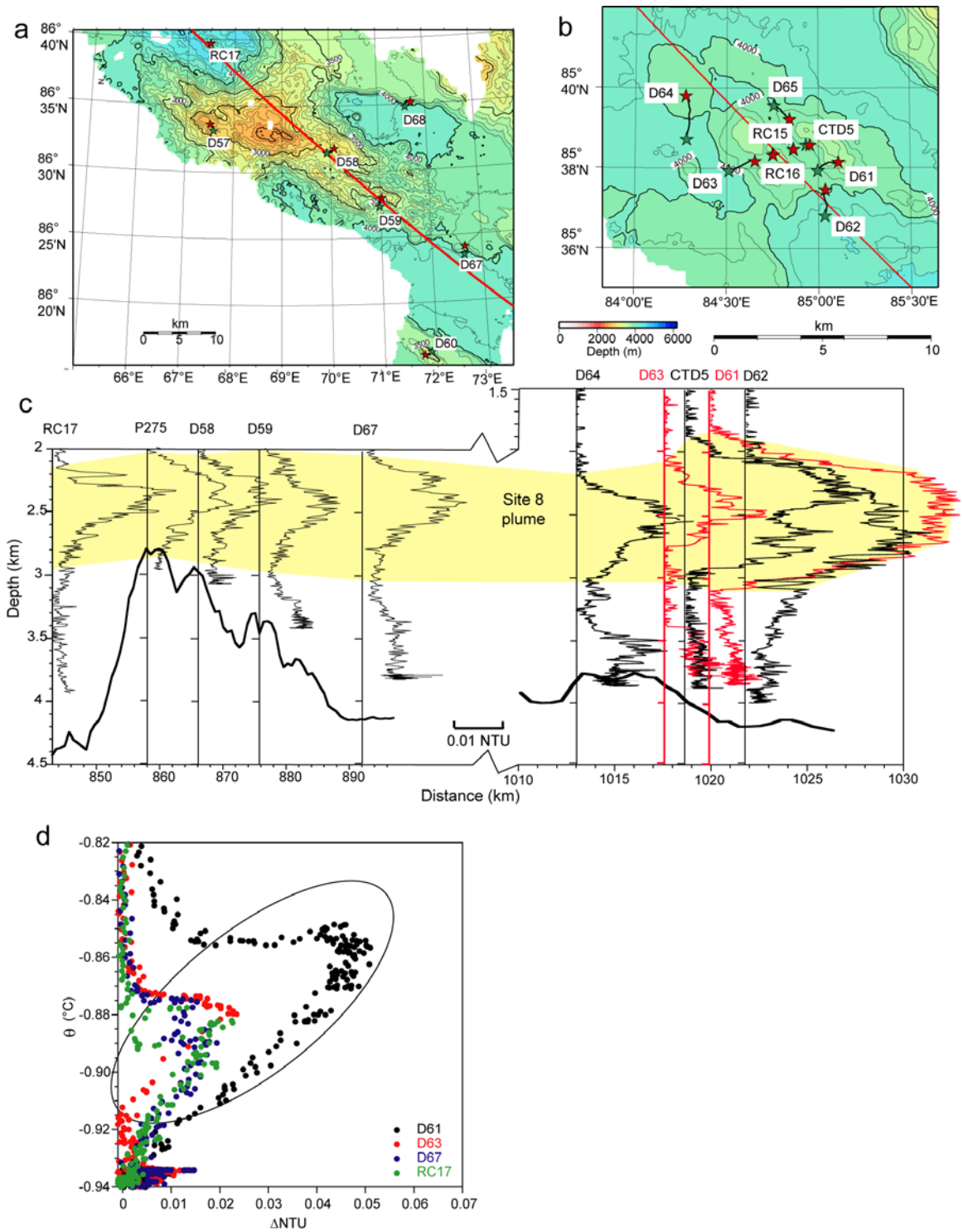

Figure 15. Location maps for the volcanic edifice at (a) 69°E and (b) the site 8 region. Plume ΔNTU profiles across both regions are shown in Figure 15c. Symbols, map characteristics, and legend are as in Figure 7. Note the break in distance scale in Figure 15c. (d) θ/ΔNTU ratios remain constant within the site 8 plume over the entire 175 km distance displayed here.

months-long volcanic eruption occurred on the valley floor in 1999. More than 2.5 yr after the first seismic events, fluid discharge remained sufficient to sustain a plume 700–1500 m thick over the volcanic mound and extending some 170 km westward along the axial valley and unknown distances in other directions.

[31] We can roughly inventory the hydrothermal heat within the near-source plume by assuming that the cross section in Figure 15 (D64 to D62) represents a representative slice through an oblate spheroid plume with a nominal diameter of 10 km and a maximum thickness of 1.1 km (for a contoured plume section, see Figure 4 of *Edmonds et al.* [2003]). The excess (hydrothermal) heat in this plume core is $\sim 7.5 \times 10^{15}$ J. The source heat flux required to maintain such a plume could be estimated if we knew the plume renewal rate. No near-bottom flow measurements are available from the central Eurasian Basin, but a recent diagnostic model predicts bottom geostrophic velocities of <1 cm/s around the Gakkel Ridge [*Nost and Isachsen*, 2003]. For a hypothetical mean current of 0.5 cm/s, the plume directly overlying site 8 would be completely flushed away within about 24 d if not resupplied by steady venting. Maintaining the plume would require a source heat flux of (7.5×10^{15} J)/24 d, or ~3600 MW; faster or slower mean currents would increase or decrease this flux proportionally. A 3600 MW output is substantial but not unreasonable. The heat flux from the large MAR vent fields at Rainbow (36°15′N, 33°53′W) and TAG (26°08′N, 44°50′W), for example, have been measured as 1000–5000 MW [*Thurnherr and Richards*, 2001] and 500–940 MW [*Rudnicki and Elderfield*, 1992], respectively. While our estimate is more poorly constrained, it nevertheless supports the inference of a major hydrothermal field at this location.

[32] How convincing is the evidence that the 69°E plumes originate at 85°E? With no plume profiles between the two areas or opportunity to compare chemical signatures (water samples were collected at 85°E but not at 69°E), we can rely only on indirect evidence. No volcanic centers were mapped between 73°E and 85°E, so the likelihood of an unsampled site producing the 69°E plume is minimal. A westward advection from site 8 is consistent with a westward extension of plumes from sites 4 and 5, with the large-scale temperature distribution (Figure 4), and with models of the deep circulation [*Jones et al.*, 1995; *Nost and Isachsen*, 2003]. Figure 15 demonstrates the congruity of plumes at 69°E and 85°E, and shows that the θ/ΔNTU values in the plume maximum remain constant for at least 175 km. With the recovery of fresh glassy pillow basalt at the 69°E edifice, we do not dismiss the possibility that it, along with those at 19°, 37°, 43° and 55°E, is hydrothermally active, but prefer the simpler explanation of a single site at 85°E.

4.10. Gakkel Ridge Summary

[33] The available plume evidence supports a minimum of eight located and one unlocated sites that produce detectable optical and thermal plume anomalies. Three lie in the Western Volcanic Zone, two in the Sparsely Magmatic Zone (though the location of the 2°–19°E plume source is unknown), and four in the Eastern Volcanic Zone. With the exception of the Sparsely Magmatic Zone sites, all known sites occur in association with basaltic mounds or crust. The areal scale of each of these sites is not well constrained, though they apparently vary from extensive (site 8) to petite (site 3). The volcanic edifice at 69°N, the only large construct in the Eastern Volcanic Zone lacking an identified source, may support a tenth site. Additional vent fields, especially small ones, may have gone unobserved.

[34] These handful of identified active sites support an almost continuous plume presence with two distinct geometries: local plumes detectable no more than a few to ~10 km from their apparent source (sites 1, 2, 3, 6, 7), and extensive plumes advected coherently for >100 km along the rift valley (from sites 4, 5, 8, and the source of the 2°–19°E plume (likely long-lived faults on the valley wall)). Local plumes are shallow (<3000 m) (sites 2, 3, 6, 7), laterally constrained by bathymetry (site 1), and/or relatively weak (sites 1, 3). Shallow plumes, especially at sites 6 and 7, rise above the bounding flank walls and can thus be readily dispersed off axis. The along-axis extent of each of these plumes, ~10 km, is similar to those from isolated vent fields on other ridges [e.g., *Baker et al.*, 1995; *German and Parson*, 1998; *German et al.*, 1998a; *Bach et al.*, 2002].

[35] The four extensive plumes identified here (2°–7°E (site 4), 2°–19°E (unknown site), 19°–42°E (site 5), and 67°–85°E (site 8)) each persist for 100–200 km and by themselves overlie almost half of the entire surveyed ridge. The western three are confined below the maximum height of the valley walls along that section of ridge (Figure 4b).

The observed intensity and thickness of each varies moderately along the ridge, presumably because the scattered station locations did not follow the plume axis, or because local currents disrupt the continuity of the plume. The 67°–85°E extensive plume is different in two related ways: the plumes at the apparent source area (site 8) are the most intense and voluminous anywhere on the Gakkel Ridge, and these plumes rise well above any bounding valley walls [*Coakley and Cochran*, 1998; *Cochran et al.*, 2003; *Brozena et al.*, 2003] (Figure 4b). We suggest that the apparently massive hydrothermal discharge at site 8, combined with the postulated regional westward drift of deep water over the Gakkel Ridge [*Nost and Isachsen*, 2003], are sufficient to maintain the coherence of this plume for at least 175 km even without the aid of an axial valley corridor.

[36] Such long-distance plume continuity is not unique to the Gakkel Ridge. On the MAR, the Rainbow plume meanders recognizably along the AMAR segment for up to 50 km [*German et al.*, 1998b; *Thurnherr et al.*, 2002] downcurrent of its source. The detailed plume mapping of *German et al.* [1998b] also revealed that such a plume need not fill the entire valley width. Along-axis currents tend to carry the plume along isobaths, so that its thickness, intensity, and even detection vary along the valley. Plume confinement on slow- and ultraslow-spreading ridges may have important consequences for the dispersal potential of larvae from hydrothermal habitats. Dispersal success is directly related to the efficiency of advective transport between vent sites, and the off-axis component of flow sharply limits the along-axis distance achievable by larvae [*Marsh et al.*, 2001]. While flow velocities are likely low within the Gakkel Ridge valley, larvae entrained in axis-confined plumes may enjoy a high probability of passing over another hospitable habitat.

[37] The plume incidence factor, p_h, the fraction of ridge length overlain by hydrothermal plumes, is commonly used as a measure of the relative frequency of hydrothermal activity [*Baker and Hammond*, 1992; *Baker et al.*, 1996]. The highest p_h values previously found for large-scale surveys were ~0.6 along two sections of the superfast spreading East Pacific Rise [*Urabe et al.*, 1995; *Baker et al.*, 2002]. The prevalence of extensive plumes on the Gakkel Ridge results in the highest p_h yet documented. Equating p_h to the fraction of MAPR profiles that detected a hydrothermal plume (as employed by *Scheirer et al.* [1998]) yields a value of 0.82; a slightly smaller but more representative value of 0.75 is obtained from the fraction of axial length overlain by the plumes in Figure 4, not including the 20°15′–24°40′E and 72°42′–84°17′E sections where no stations were occupied. We discuss the significance of this high p_h value in section 6.

5. Southwest Indian Ridge Plume Distributions

[38] Detailed bathymetry and plume locations in the eastern SWIR have been presented by *German et al.* [1998a], so we only briefly review those results here. These areas are the only ultraslow ridge sections where plumes have been mapped using a continuous tow method. The parallel tow tracks through each section, using multiple MAPRs, detected a total of 10 optical anomalies with distinct geographical limits, located in six separate areas (Figure 6). In each case the plumes were laterally continuous and well above-bottom, strongly indicative of hydrothermal rather than erosional origins. Direct calculation of p_h using the tow data yields a value of 0.12.

[39] Interpretation of the MAPR profiles from the western SWIR is more tentative, owing to the hydrological complexity and widespread resuspension described earlier. Initial results from the oblique supersegment were described by *Bach et al.* [2002]. Here we review the geologic settings of candidate plumes identified in that paper, plus those identified using an additional 46 profiles collected on the 2000/01 and 2003 cruises.

[40] We are most confident about three sites in the oblique supersegment, detected by D54–D56 (Figure 16), D36 (Figure 17), and D82 (Figure 18). The first area was discussed in detail by *Bach et al.* [2002]. D54, one of a series of four dredges along the base of the southern rift valley wall in this area, showed a strong ΔNTU and coincident θ layer from 3700–4100 m, including near-bottom temperature anomalies observed while dredge haul traversed the seafloor. This plume is the strongest hydrothermal indicator yet found on the western SWIR. D36 found a weak near-bottom ΔNTU layer above pillow lavas on the NE wall of an axial ridge just east of the largest volcano on the western SWIR. D82 (an empty dredge), at the eastern end of the supersegment in a short amagmatic segment, mapped an intense ΔNTU layer ~400 m thick and ~100 m above bottom near the intersection of an axial ridge and the northern rift

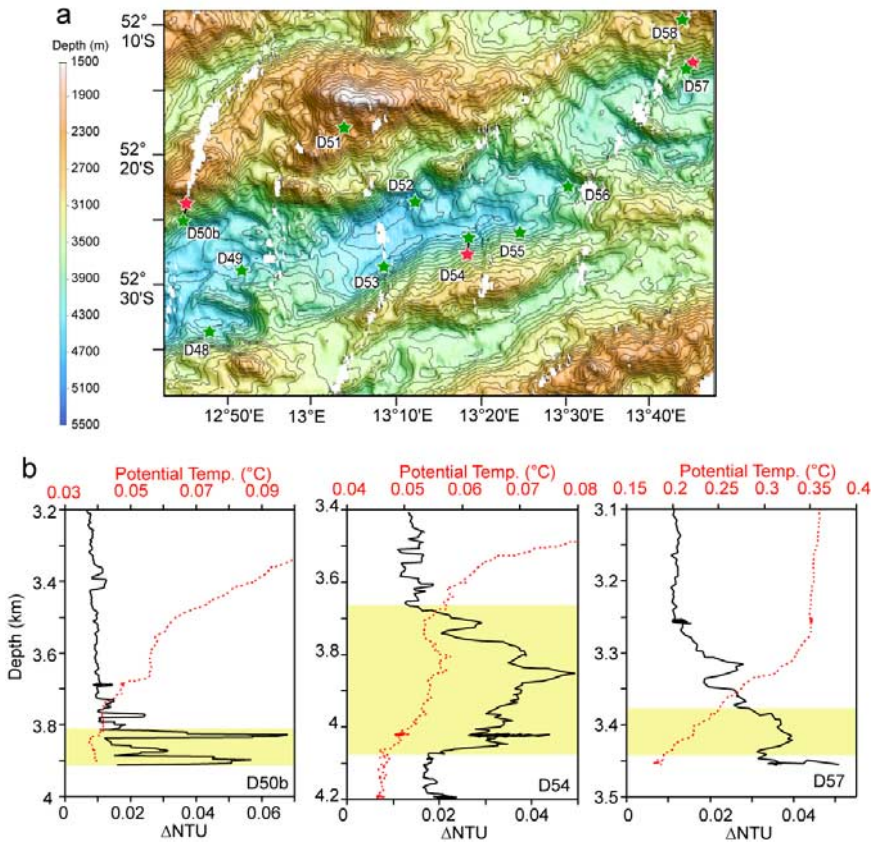

Figure 16. (a) Location of D50b, D54, and D57 in the oblique supersegment. Green stars show the ship location at the start of the dredge, and red stars show the location at the end. Other dredges in this area are shown only by the green stars. D55 and D56 also detected the plume apparently emanating from the D54 area [see *Bach et al.*, 2002]. Contour interval equals 100 m. (b) ΔNTU (black solid line) and θ (red dotted line) profiles at the three most likely hydrothermal sites. Yellow bands indicate possible hydrothermal plumes. Note the strong positive inflection in the θ profile in the D54 plume.

valley wall. A slight positive inflection in the θ profile also occurs at the plume maxima.

[41] Three other ΔNTU anomalies of possible hydrothermal origin were detected in the oblique supersegment. Multiple intense but thin near-bottom scattering layers were present on D50b (Figure 16), a dredge at the base of the north valley wall that recovered only ultramafic rocks. A much weaker near-bottom plume (~3400 m) was present on D57 (Figure 16), located near an E–W-striking portion of the northern rift valley wall. The shallower ΔNTU anomaly at ~3300 m, just above a strong θ gradient, is likely a product of the local hydrography. Finally, D62 (Figure 18) mapped another weak ΔNTU layer, ~100 m above bottom, adjacent to a normal fault face cutting an oblique section of the southern rift valley wall.

[42] On the longer and more volcanic orthogonal supersegment only two profiles are possible hydrothermal candidates, and neither is compelling. D9b, in the center of the axial valley between two volcanic edifices, found a strong near-bottom plume (Figures 19a and 19b). The plume occurs within a θ minimum and could be resuspended particles carried by the thin bottom layer of inflowing colder water rather than local hydrothermal precipitates. D20, also between two volcanic edifices, was located on the south side of a low volcanic construct in the axial valley center (Figures 19c and 19d). It recorded thin, weak, but distinct layers ~200 m above bottom that are not related to any obvious hydrographic features.

[43] Perhaps the most surprising result from the western SWIR is that the oblique supersegment, with possibly the lowest effective spreading rate (7.8–12.4 mm/yr) on the global ridge system and a near non-existent basaltic crust, hosts six of the eight possible hydrothermal sites. On the orthogonal supersegment, with up to twice the spreading rate (14.4 mm/yr) and abundant volcanic features, we found only weak evidence at two sites. This differ-

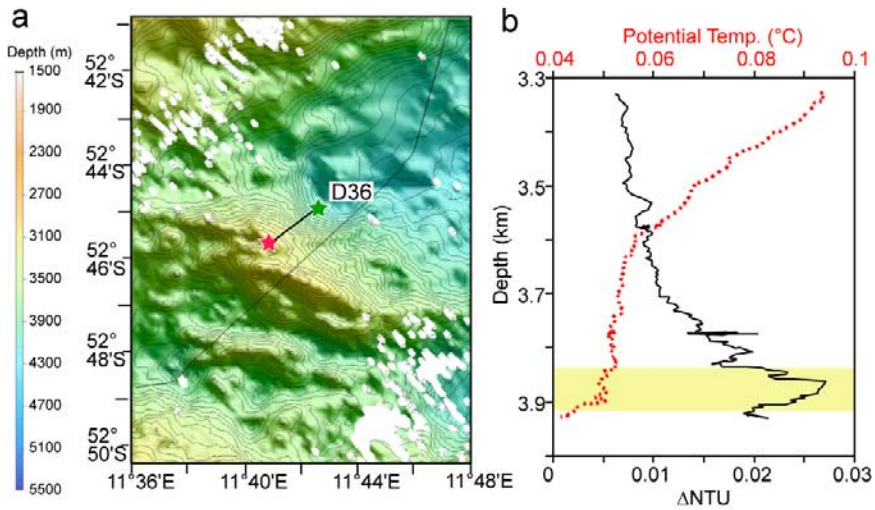

Figure 17. (a) Location of D36 on the north side of a volcanic ridge in the axial valley of the oblique supersegment. The green star shows the ship location at the start of the dredge, and the red star shows the location at the end. Contour interval equals 50 m. (b) ΔNTU (black solid line) and θ (red dotted line) profiles at D36. The yellow band indicates a possible hydrothermal plume.

ence is remarkable even considering that the mean profile spacing on the orthogonal supersegment (16.5 km) is twice that of the oblique supersegment (7.8 km). Also, and in sharp contrast to the Gakkel Ridge, we observed no plumes over the summits of any of the volcanoes on either supersegment.

[44] Because of differences between these two supersegments we calculate separate statistics for each. On each section, p_h can be calculated from the percentage of vertical MAPR profiles that recorded a plume, a valid method where no extensive plumes bias the data [*Scheirer et al.*, 1998]. Of the 55 profiles collected from 10° to 16°E, at least 7 and a maximum of 9 detected hydrothermal plumes, yielding a p_h of 0.11 to 0.16. These profiles represent three to six separate hydrothermal sites, a population size supported by recovery of fossil hydrothermal deposits in 6 of 38 dredges, including massive sulfides from the rift valley walls [*Bach et al.*, 2002]. Of the 32 profiles collected from 16° to 23°E, 0–2 profiles may have sampled plumes, so p_h = 0–0.06. The combined p_h estimate for the entire western SWIR, 0.07–0.13, encompasses the value of 0.12 calculated for the eastern SWIR.

6. Discussion

[45] These new data from ultraslow ridges make it possible for the first time to examine the relationship between hydrothermal activity and spreading rate over the entire global MOR spectrum. Ideally, we wish to know how the total hydrothermal heat output varies with spreading rate, but vent-field-scale heat flux measurements are difficult, imprecise, and will remain rare for the foreseeable future. Our only current alternative is to use surrogate measures such as p_h and vent field frequency. On fast spreading ridges, plume surveys are generally spatially continuous (e.g., CTD tow-yos, towed MAPR arrays) and plumes readily disperse off-axis, unimpeded by axial bathymetry. Determination of p_h is thus straightforward and appears indicative of the spatial frequency of venting [*Baker et al.*, 1995, 1996; *Baker and German*, 2004]. On slow-spreading ridges, however, rift valleys can be confining, making individual plumes detectable for <10 to >100 km along axis, and plume surveys have generally been discontinuous (such as the AMORE and western SWIR work). Calculation of p_h can thus be imprecise and even misleading. Enumerating individual vent fields eliminates the confounding role of plume dispersion or confinement in assessing relative hydrothermal activity, but has its own difficulties. On slow ridges vent fields tend to be large and isolated [e.g., *Wilcock and Delaney*, 1996] so counting them seems tractable. As spreading rate increases fields become smaller, their boundaries increasingly indistinct and difficult to discern from

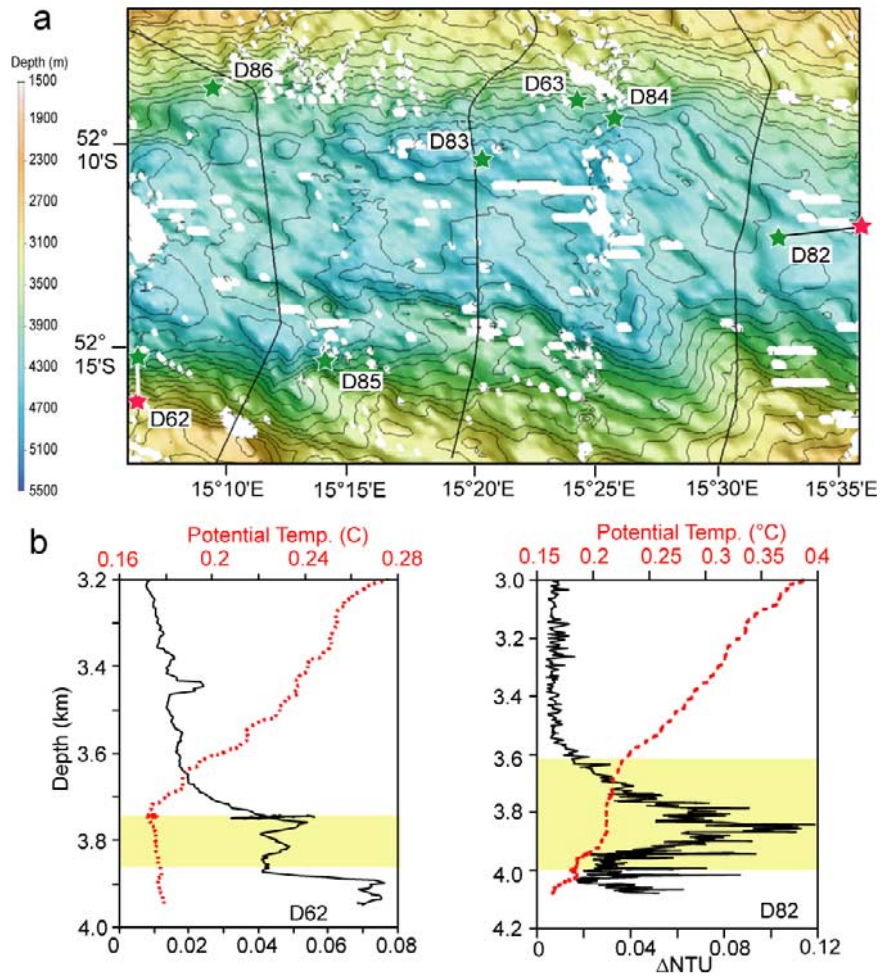

Figure 18. (a) Location of D62 and D82 at the eastern end of the oblique supersegment. Green stars show the ship location at the start of the dredge, and red stars show the location at the end. Other dredges in this area are shown only by the green stars. Contour interval equals 100 m. (b) ΔNTU (black solid line) and θ (red dotted line) profiles at D62 and D82. Yellow bands indicate possible hydrothermal plumes. The θ profile in the D82 plume appears to have a slight positive inflection within the plume.

plume mapping, and even the concept of discrete fields suspect.

[46] We begin by comparing the sampling strategy at each of the three ultraslow ridge sections to assess the confidence of those results. Along the eastern SWIR (Figure 20a), a set of MAPRs attached to the wire of a deep-tow side scan package continuously surveyed a 300-m thick layer ~100 to 500 m above the bottom. A similar survey conducted along the Gakkel Ridge (Figure 20c) might have detected most of the plumes AMORE located, but would have provided no inkling of the extensive plume coverage there. Along the western SWIR (Figure 20b), the MAPR campaign was analogous to AMORE but with a mean profile spacing almost twice as great (10.9 versus 6.6 km), sufficient to document extensive plumes but perhaps marginal to consistently detect localized plumes with a lateral scale of ~10 km (Figure 20c).

[47] Both the deep-tow and vertical profile approaches have strengths and weaknesses. Towing the axial valley, especially the dual parallel tows used on the eastern SWIR, can readily detect even localized plumes provided they intersect the tow swath. Keeping the tow body at a more uniform height above the seafloor and expanding the swath vertical thickness by adding additional sensors would afford great improvement in this approach. Vertical profiles will detect plumes at any height, but their effectiveness is a direct function of their spatial density and distribution,

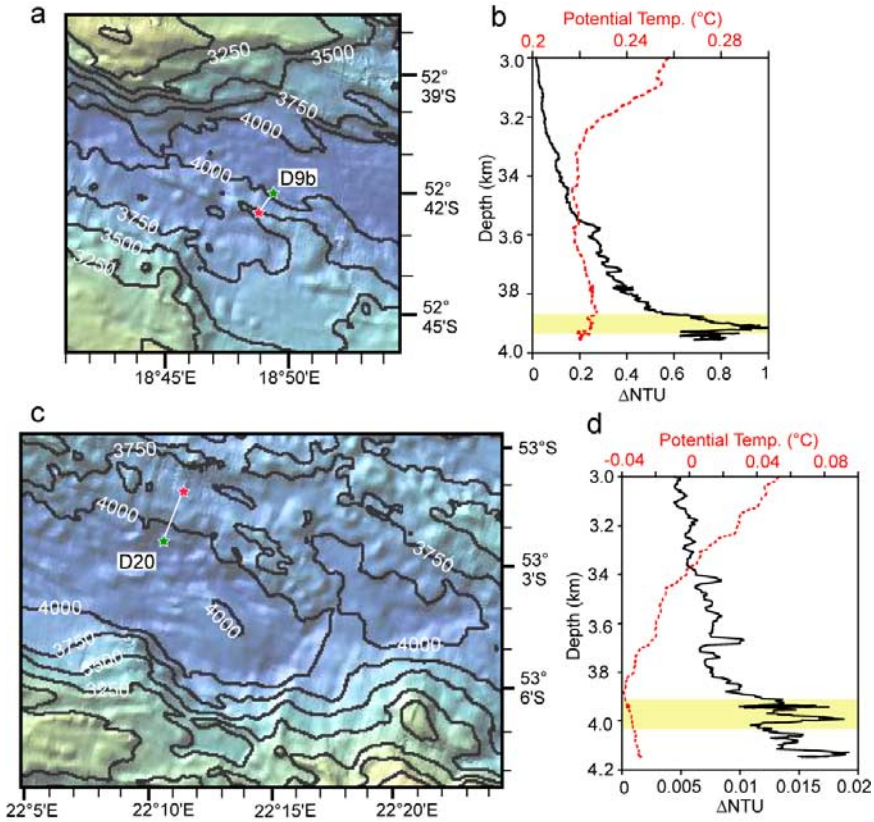

Figure 19. (a) Location of D9b in the axial valley of the orthogonal supersegment. The green star shows the ship location at the start of the dredge, and the red star shows the location at the end. (b) ΔNTU (black solid line) and θ (red dotted line) profiles at D9b. The yellow band indicates a possible hydrothermal plume. (c) Location of D20; symbols as in Figure 19a. (d) ΔNTU and θ profiles at D20; legend as in Figure 19b. The bathymetry in this figure is from the GeoMapApp database at http://data.ridge2000.org/.

as generally dictated by rock sampling rather than plume mapping.

[48] For the Gakkel Ridge, we consider the coverage excellent owing to the high density of profiles and a hydrography that permits plumes to rise above both the topography and the confounding effect of resuspended sediments. In this particular environment a deep-tow survey might have provided less plume information. Both the SWIR surveys had poorer, but still useful, coverage. On the western SWIR (Figure 20b) the discontinuous profile coverage was sufficient to demonstrate the absence of extensive plumes. Detection and identification of near-bottom hydrothermal plumes, however, was complicated by the high incidence of thick bottom nepheloid layers, presumably indicative of sediments resuspended by deep water intruding from the bounding transform faults. On the eastern SWIR (Figure 20a), the continuous deep-tow survey was probably effective in detecting deep, localized plumes. However, any plumes above or below the swath went unobserved. While the AMORE survey was best, we regard the coverage in each of the SWIR sections sufficient for comparison with the Gakkel Ridge data.

[49] To place ultraslow ridges in the global context, we first add the p_h results to existing data from faster-spreading ridges and plot against the spreading rate of each surveyed ridge section (Figure 21a). Because of the fundamental difference in the geology of the oblique supersegment (10°–16°E) compared to the orthogonal supersegment (16°–23°E) in the western SWIR we plot these segments separately. Except for the Gakkel Ridge, these data yield a robust linear relation with an intercept close to zero. (We do not consider here hot spot-affected ridges such as the Reykjanes Ridge and the Southeast Indian Ridge overlying the Amsterdam-St. Paul hot spot [see *Baker and German*, 2004].) The consistency of this trend implies that, in many

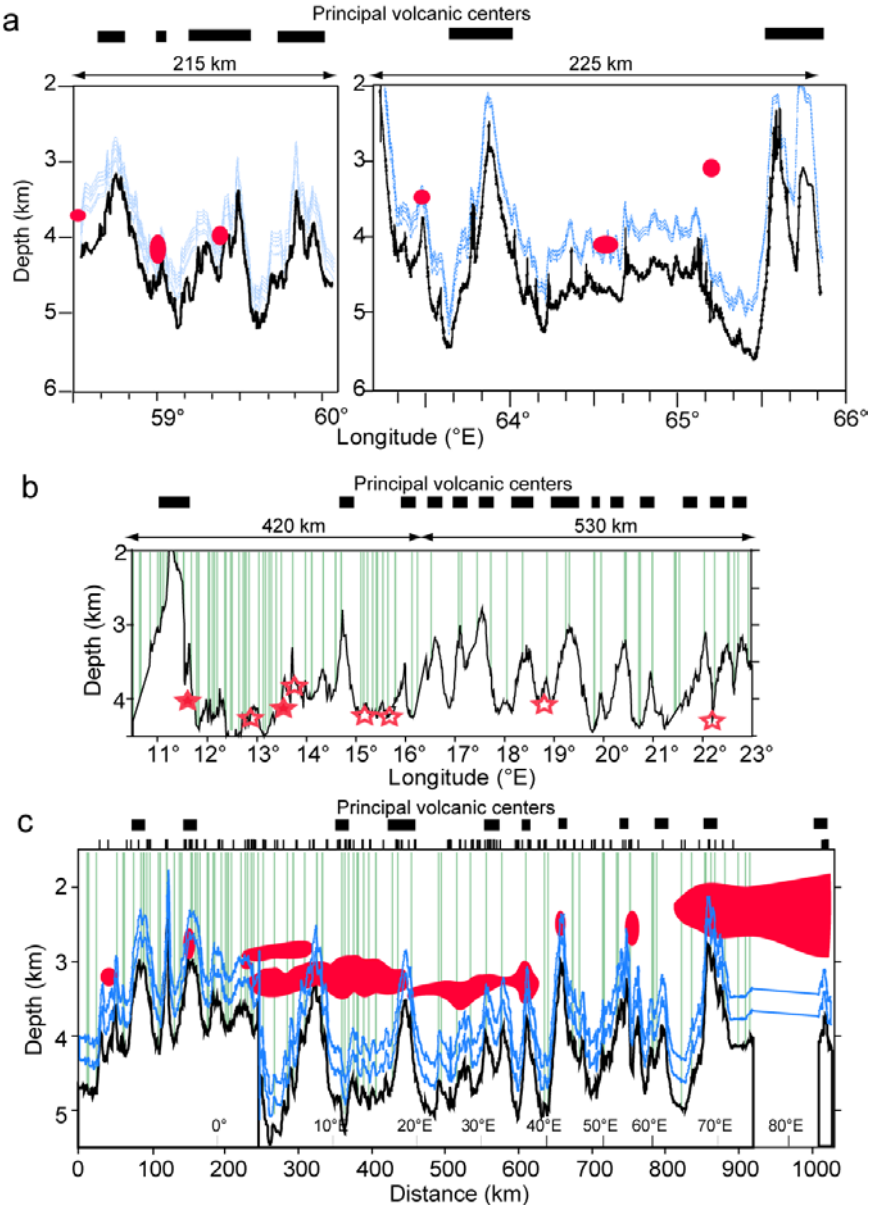

Figure 20. Schematic comparison of plume distribution and sampling strategies along the (a) eastern SWIR, (b) western SWIR, and (c) Gakkel Ridge. Vertical and horizontal scales are the same for each section, except that the horizontal scale in Figure 20a is expanded to show detail. Heavy bars at the top of each panel indicate approximate extent of local magmatic centers/volcanic constructs. In Figure 20a the MAPR paths (light blue lines) intersected six incidences of optical anomalies (red ellipses) while following the bathymetry (heavy black line). The MAPRs traced a variable height above bottom, depending on the elevation of the side scan package. This diagram shows only one of two parallel tracks; the plume at 65°10′E was detected on the other track, which followed a slightly different bathymetry. In Figure 20b the MAPR profiles (green lines) were scattered along the axial valley, with at least one profile located over every volcanic center. In Figure 20c we indicate how effectively the sampling strategies in Figures 20a and 20b would locate the Gakkel Ridge plumes (solid red shapes). The deep-tow strategy is mimicked by superimposing hypothetical MAPR paths (light blue lines) spanning 400–700 m above bottom. Extensive plumes would have been poorly sampled. A vertical profile distribution like that in Figure 20b (green lines) might have missed some localized plumes but would have easily detected the extensive plumes.

ridge environments, advective dispersion of plumes is similar and the along-axis extent of plumes is a first-order indication of the seafloor extent of discharge sites. The Gakkel Ridge environment is a notable exception. The dramatic offset of the Gakkel Ridge from this trend is a cautionary, though extreme, example of the effect that hydrography and plume confinement in deep axial valleys can exert on p_h. Note, too, that no lengthy slow-spreading (20–50 mm/yr) ridge sections have been surveyed adequately enough to calculate p_h.

[50] To avoid the problems associated with an inferential index such as p_h, we can plot vent field frequency, F_s (sites/100 km of ridge length), against spreading rate. We detected 9–10 vent fields along the 850 km of surveyed Gakkel Ridge, so F_s = 1.1–1.2. The continuous tow data recorded along 440 km of the eastern SWIR (58°–66°E) found six sites (F_s = 1.3). Results from the western SWIR have a higher uncertainty because of the complexity of the ΔNTU profiles. On the western SWIR 10°–16°E section, our estimate of 3–6 sites yields an F_s = 0.7–1.4, while the estimate of 0–2 sites on the 16°–23°E section yields F_s = 0–0.4. Plotting these ultraslow ridge sections along with values for faster-spreading ridges (Figure 21b) (see *Baker and German* [2004] for details of the F_s calculations) results in a scattered distribution that reflects not only the observed distribution of hydrothermal activity but also the current intensity of seafloor exploration effort and the uncertainty in enumerating vent fields. To improve the statistics we bin the individual ridge sections into five spreading rate categories to achieve a minimum ridge length of >500 km (Figure 21d) for each data point. A least squares fit to these five points produces a trend as robust as that for p_h, but now including the Gakkel Ridge data (Figure 21b).

[51] While the first-order trend for both p_h and F_s shows a linear relation to spreading rate, the fact that the magma budget decreases more abruptly than the spreading rate at ultraslow ridges [*Reid and Jackson*, 1981; *White et al.*, 2001] suggests that ultraslow ridges are more efficient producers of vent fields than other ridges. We can test this hypothesis by normalizing F_s to the time-averaged delivery of magma. To normalize F_s we calculate F_m, the site frequency per 1000 km^3 magma per Myr, for each spreading rate bin as

$$F_m = 10^3 \mathrm{N}/(\mathrm{L}u_s\mathrm{T_c}), \quad (2)$$

where for each bin N = number of vent fields observed, L = ridge length (km), u_s = weighted average full spreading rate (mm/yr), and T_c = crustal thickness. For ultraslow ridges we use a nominal thickness of 4 km [*Muller et al.*, 1999; *Jokat et al.*, 2003], except for the oblique supersegment of the western SWIR, where dredging indicates a crustal thickness of <1 km [*Dick et al.*, 2003]. We assign a 6.3 km thickness to all other ridges [*White et al.*, 1992, 2001]. F_m steadily increases from superfast to slow ridges then increases sharply for ultraslow ridges (Figure 21c).

[52] On the basis of the geology of ultraslow-spreading ridges, is a substantial increase in F_m a supportable conclusion? The primary controls on vent distribution along any ridge section are heat source and permeability, but the relative importance of each remains uncertain [e.g., *Fornari and Embley*, 1995; *German and Parson*, 1998; *Baker et al.*, 2001]. Bulk permeability may increase as spreading rate increases and faults become deeper and longer-lasting, but no quantitative estimates of such a trend exist. Thus we focus here on the principal heat sources available to drive hydrothermal circulation: basaltic magma delivered to the crust and, especially at slow and ultraslow ridges, gabbroic intrusions and cooling of rising mantle peridotite.

[53] A hallmark of ultraslow-spreading ridges is amagmatic segments with minimal or no basaltic crust [*Dick et al.*, 2003]. On the Gakkel Ridge, basaltic rocks are generally absent from 3°–13°E, as they are from 11°45′ to 14°15′E and 15° to 15°45′E on the SWIR [*Dick et al.*, 2003]. Seismic refraction measurements yield crustal thicknesses of only 1–4 km between 10°E and 50°E on the Gakkel Ridge [*Coakley and Cochran*, 1998; *Jokat et al.*, 2003], and a mean of only 4 km between 65°30′ and 66°42′E on the SWIR [*Muller et al.*, 1999]. Within such thin crust, much of the basaltic heat is likely lost quickly to seawater during eruptions and shallow intrusions, and the durable heat reservoirs needed to sustain venting might be scarce. However, as spreading rate declines magma delivery becomes increasingly three-dimensional [*Lin and Phipps Morgan*, 1992], constructing massive volcanic edifices with along-axis relief reaching 2 km on ultraslow-spreading ridges (Figure 20).

[54] Where focused volcanic activity accumulates basalt, melt reservoirs may grow large enough to increase the efficiency of the magma budget and sustain long-lasting hydrothermal circulation. On the Gakkel Ridge, every detected vent site in the Eastern Volcanic Zone is associated with one of

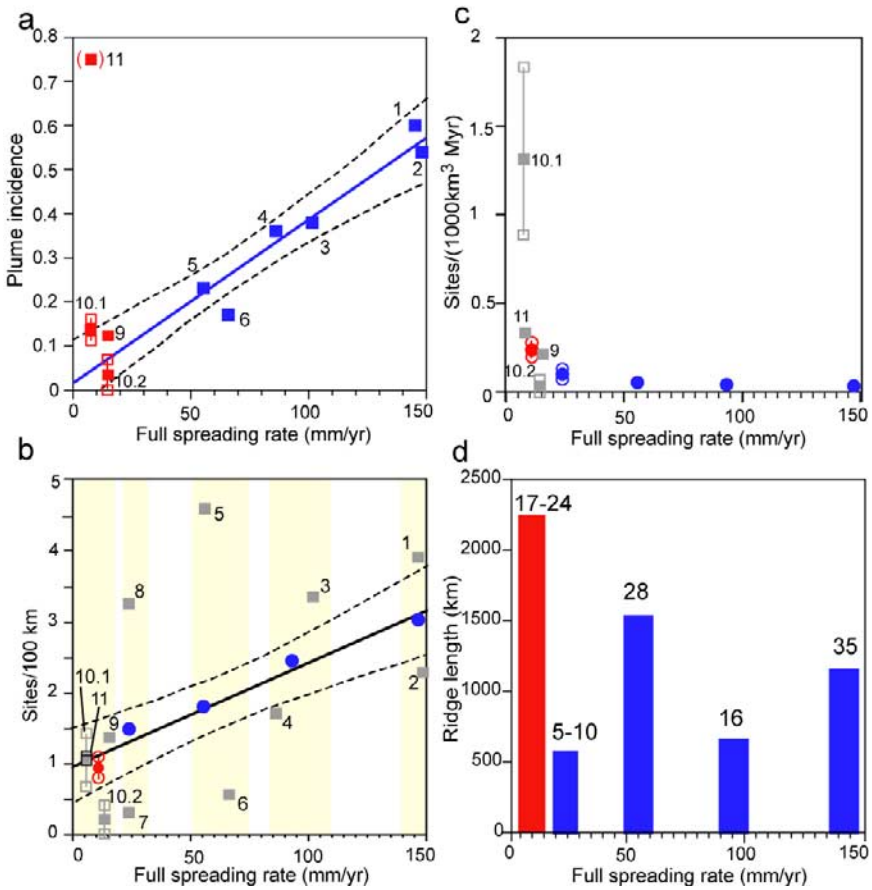

Figure 21. (a) Plume incidence for selected ridge sections where these statistics have been compiled (not including hot spot-affected Reykjanes and Southeast Indian Ridges) (solid symbols indicate mean value, and open symbols indicate minimum and maximum estimates, where applicable: red for ultraslow ridges and blue for all others). Reported plume incidences include 1, EPR 13°–18°S [*Urabe et al.*, 1995]; 2, EPR 27°–32°S [*Baker et al.*, 2002]; 3, EPR 9°–13°N [*Baker et al.*, 1994]; 4, EPR 15°–18°N [*Baker et al.*, 2001]; 5, JDFR [*Baker and Hammond*, 1992]; 6, Southeast Indian Ridge, 77°–88°E [*Scheirer et al.*, 1998; *Baker and German*, 2004]; 9, western SWIR [*German et al.*, 1998a; *Baker and German*, 2004]; 10.1 and 10.2, oblique and orthogonal supersegments, respectively, of eastern SWIR [*Bach et al.*, 2002; this paper]; 11, Gakkel Ridge. (b) Site frequency (gray squares), F_s (number/100 km), from the same sections, plus 7, MAR 27°–30°N [*Murton et al.*, 1994]; 8, MAR 36°–38°N, data from many studies summarized by *Baker and German* [2004]. Blue and red circles show data binned into five spreading rate categories (yellow bands). In Figures 21a and 21b a least squares regression fit (solid line; dotted lines show 95% confidence limits) is shown for ridge sections 1–6 and 9–10 only in Figure 21a ($y = 0.032 + 0.0036x$, $r^2 = 0.93$) and the five binned groups only in Figure 21b ($y = 0.98 + 0.015x$, $r^2 = 0.96$). (c) Site frequency normalized to the magma delivery rate (sites/(1000 km^3 Myr)) versus spreading rate. Symbols are as in Figure 21b, but only ultraslow individual segments are shown. (d) Total length of ridge surveyed and number of vent sites detected in each bin. More vent sites are known than are indicated here [see *Baker and German*, 2004], but these figures include data only from well-surveyed ridge sections.

these edifices, and sites 1 and 2 in the Western Volcanic Zone occur on smaller axial volcanic ridges. On the eastern SWIR, an extinct high-temperature vent field sits atop Mount Jourdanne at 63°56′E (Figure 20a) [*Münch et al.*, 2001]. Focused volcanism may greatly increase the efficiency of meager basalt resources in producing and sustaining hydrothermal discharge, increasing the apparent efficiency of the magma budget and leading to the higher F_m values calculated here.

[55] Magmatic focusing is insufficient to explain all venting on ultraslow ridges, however, as plumes were absent over most volcanic edifices on the SWIR. On the western SWIR in fact, suspected vent sites are concentrated in the

two amagmatic segments between 11° and 16°E (Figure 5). These sites may be maintained by non-basaltic heat sources, such as cooling of gabbroic intrusions, upwelling mantle peridotite, and serpentinization, accessed by enhanced permeability created by long-lived and deep fault planes. For example, the strongest plume on the western SWIR, at ~13°20′E (Figure 16), was found along the wall of a large fault block with a 1200 m footwall extending from valley floor to the crest of the rift valley wall [*Bach et al.*, 2002]. Hydrothermal deposits in the western SWIR were primarily found on the rift valley walls, further emphasizing the role of tectonism over volcanism in controlling hydrothermal activity there [*Bach et al.*, 2002; *Dick et al.*, 2003]. If the degrees of mantle melting are very small, such as at the SWIR 14–16°E [*Salters and Dick*, 2002], the heat of fusion is largely retained and thus available to drive hydrothermal circulation. Recent drilling at 14°–16°N on the MAR, for example, suggests that the crust/lithosphere there may be 25% gabbroic [*Kelemen*, 2003], and crystallization of such rocks at depths to 20 km might provide a sizable deep heat source in basalt-poor ridge segments. *Cannat et al.* [2004] calculate that upwelling of mantle peridotite on magma-starved ridge segments could supply 16 MW/km of axis (at u_s = 25 mm/yr), little different than their estimate of 18–25 MW/km for a magmatically dominated segment of the same spreading rate. Ultraslow-spreading ridges may thus have substantial deep heat sources available to power hydrothermal circulation, creating more vent fields than expected from their weak magma budget and low spreading rate. Serpentinization may also provide supplemental heat to conventional basaltic/gabbroic-hosted hydrothermal circulation, as apparently occurs at the MAR Rainbow site [*Charlou et al.*, 2002; *Douville et al.*, 2002], though *Cannat et al.* [2004] figure it may contribute only ~5% of the total heat supply.

[56] One question that remains unanswered is why the apparent pattern of geological control on venting seems so different between the Gakkel Ridge, where most sites are associated with volcanic edifices, and the SWIR, where most sites occur in the amagmatic segments. Until we know the precise geological setting of many of these sites we can do little more than speculate, but the difference may simply be a manifestation of cyclical patterns with timescales on the order of 10^4–10^6 yr. *Cannat et al.* [2003] suggest that along the eastern SWIR (61°–69°E) melt distribution is more variable in time than on the MAR, with enhanced episodes of melt supply lasting only ~10–15% of the last 10 Myr.

7. Conclusions

[57] Temperature/optical profiles collected at 145 dredge, rock core, CTD, and camera stations on the ultraslow-spreading Gakkel Ridge found a plume incidence (p_h) of ~0.75, higher than on any other multisegment ridge section yet surveyed, regardless of spreading rate. Unlike most other studied ridge sections, however, p_h on the Gakkel Ridge is not an accurate indicator of the spatial frequency of hydrothermal vent sites. A capacious axial valley, vent site locations on highstanding volcanic centers, and a nearly isopycnal water column below 3500 m enable some plumes to disperse coherently for up to 200 km from their source. Detailed mapping of the plume distributions finds evidence for only 9–10 vent sites in 850 km of survey ridge, at least 6 of which are associated with volcanic centers. For the Gakkel Ridge, we thus calculate a site frequency, F_s, sites/100 km of ridge length, of 1.1–1.2.

[58] Plume distributions are fundamentally different along the eastern and western SWIR. No plumes have been found above prominent volcanic centers, and a normal deep-ocean density gradient inhibits plume rise, so no extensive plumes are apparent. The p_h value for the two SWIR areas ≈0.1, consistent with the linear trend hypothesized for faster-spreading ridges. The F_s value for each area ≈1, in agreement with the Gakkel Ridge results. To the first order, then, F_s among the ultraslow ridge sections is comparable and also consistent with data from faster spreading ridges. However, the puzzling inconsistency of hydrothermal activity concentrated on magmatic segments on the Gakkel Ridge but on amagmatic segments of the western SWIR confirms that much remains to be learned about what controls the distribution of venting on these ridges.

[59] Normalizing F_s to the basaltic magma budget, as calculated from crustal thickness estimates, suggests that ultraslow ridges are several times more effective than faster-spreading ridges in sustaining vent fields. This efficiency may derive from some combination of three-dimensional magma focusing at volcanic centers, deep mining of heat from gabbroic intrusions and direct cooling of the upper mantle, and nonmagmatic heat supplied by exothermic serpentinization.

[60] It is important to qualify our conclusions with the reminder that they are based on hydrothermal surveys covering ~6000 km of ridge crest, only ~10% of the global mid-ocean ridge system. (The statistics are similar for ultraslow ridges; about 85% remain unsurveyed.) Even more sobering is the fact that not a single active vent field on an ultraslow ridge has been sampled, and only one, the Aurora vent field on the Gakkel Ridge, has even been precisely located and observed. Verification of the trends postulated in Figure 21, especially the remarkable efficiency of ultraslow ridges to create vent fields, will require confirmation of the vent field enumeration by seafloor observation or more comprehensive water column sampling. Our interpretations of these trends also assume that the average vent field heat flux is constant for each spreading rate category. While widespread flux measurements will not be available soon, information on the tectonic setting, size, and nature of vent fields could provide adequate data for a reliable test of our models.

Acknowledgments

[61] The authors thank M. Cannat and M. Edwards for reviews that materially improved the paper. This research was partially supported the NOAA VENTS Program. P.J.M. and H.J.B.D. gratefully acknowledge NSF grant OPP 9911795 for support of the AMORE Expedition; P.J.M. and E.T.B. acknowledge NSF grant OPP 0107767 and the VENTS Program for development and construction of MAPRs for use in ice-covered seas. H.J.B.D. acknowledges NSF grant OCE-9907630 for support of SWIR studies. J.E.S. was supported by Deutsche Forschungsgemeinschaft grant SN15/2. PMEL contribution 2672.

References

Aagaard, K., J. H. Swift, and E. C. Carmack (1985), Thermohaline circulation in the Arctic Mediterranean Seas, *J. Geophys. Res.*, *90*, 4833–4846.

American Public Health Association (1985), *Standard Methods for the Examination of Water and Wastewater*, 16th ed., 1268 pp., Washington, D. C.

Anderson, L. G., G. Björk, O. Holby, E. P. Jones, G. Kattner, K. P. Koltermann, B. Liljeblad, R. Lindegren, B. Rudels, and J. Swift (1994), Water masses and circulation in the Eurasian Basin: Results from the *Oden* 91 expedition, *J. Geophys. Res.*, *99*, 3273–3283.

Bach, W., N. R. Banerjee, H. J. B. Dick, and E. T. Baker (2002), Discovery of ancient and active hydrothermal systems along the ultra-slow spreading Southwest Indian Ridge 10°–16°E, *Geochem. Geophys. Geosyst.*, *3*(7), 1044, doi:10.1029/2001GC000279.

Baker, E. T., and C. R. German (2004), On the global distribution of hydrothermal vent fields, in *The Thermal Structure of the Ocean Crust and Dynamics of Hydrothermal Circulation*, *Geophys. Monogr. Ser.*, edited by C. German, J. Lin, and L. Parson, AGU, Washington, D. C., in press.

Baker, E. T., and S. R. Hammond (1992), Hydrothermal venting and the apparent magmatic budget of the Juan de Fuca Ridge, *J. Geophys. Res.*, *97*, 3443–3456.

Baker, E. T., and H. B. Milburn (1997), MAPR: A new instrument for hydrothermal plume mapping, *RIDGE Events*, *8*, 23–25.

Baker, E. T., R. A. Feely, M. J. Mottl, F. J. Sansone, C. G. Wheat, J. A. Resing, and J. E. Lupton (1994), Hydrothermal plumes along the East Pacific Rise, 8°40′ to 11°50′N: Plume distribution and relationship to the apparent magmatic budget, *Earth Planet. Sci. Lett.*, *128*, 1–17.

Baker, E. T., C. R. German, and H. Elderfield (1995), Hydrothermal plumes over spreading-center axes: Global distributions and geological inferences, in *Seafloor Hydrothermal Systems: Physical, Chemical, Biological, and Geological Interactions*, *Geophys. Monogr. Ser.*, vol. 91, edited by S. Humphris et al., pp. 47–71, AGU, Washington, D. C.

Baker, E. T., Y. J. Chen, and J. Phipps Morgan (1996), The relationship between near-axis hydrothermal cooling and the spreading rate of midocean ridges, *Earth Planet. Sci. Lett.*, *142*, 137–145.

Baker, E. T., M.-H. Cormier, C. H. Langmuir, and K. Zavala (2001), Hydrothermal plumes along segments of contrasting magmatic influence, 15°20′–18°30′N, East Pacific Rise: Influence of axial faulting, *Geochem. Geophys. Geosyst.*, *2*, Paper number 2000GC000165.

Baker, E. T., et al. (2002), Hydrothermal venting along Earth's fastest spreading center: East Pacific Rise, 27.5°–32.3°, *J. Geophys. Res.*, *107*(B7), 2130, doi:10.1029/2001JB000651.

Brozena, J. M., V. A. Childers, L. A. Lawver, L. M. Gahagan, R. Forsberg, J. I. Faleide, and O. Eldholm (2003), New aerogeophysical study of the Eurasia Basin and Lomonosov Ridge: Implications for basin development, *Geology*, *31*, 825–826.

Cannat, M., C. Rommevaux-Jestin, D. Sauter, C. Deplus, and V. Mendel (1999), Formation of the axial relief at the very slow spreading Southwest Indian Ridge (49°–69°E), *J. Geophys. Res.*, *104*, 22,825–22,843.

Cannat, M., C. Rommevaux-Jestin, and H. Fujimoto (2003), Melt supply variations to a magma-poor ultra-slow spreading ridge (Southwest Indian Ridge 61° to 69°E), *Geochem. Geophys. Geosyst.*, *4*(8), 9104, doi:10.1029/2002GC000480.

Cannat, M., J. Cann, and J. Maclennan (2004), Some hard rock constraints on the supply of heat to mid-ocean ridges, in *The Thermal Structure of the Ocean Crust and Dynamics of Hydrothermal Circulation*, *Geophys. Monogr. Ser.*, edited by C. German, J. Lin, and L. Parson, AGU, Washington, D. C., in press.

Charlou, J. L., J. P. Donval, Y. Fouquet, P. Jean-Baptiste, and N. Holm (2002), Geochemistry of high H_2 and CH_4 vent fluids issuing from ultramafic rocks at the Rainbow hydrothermal field (36°14′N, MAR), *Chem. Geol.*, *191*, 345–359.

Coakley, B. J., and J. R. Cochran (1998), Gravity evidence of very thin crust at the Gakkel Ridge (Arctic Ocean), *Earth. Planet. Sci. Lett.*, *162*, 81–95.

Cochran, J. R., G. J. Kurras, M. H. Edwards, and B. J. Coakley (2003), The Gakkel Ridge: Bathymetry, gravity anomalies, and crustal accretion at extremely slow spreading rates, *J. Geophys. Res.*, *108*(B2), 2116, doi:10.1029/2002JB001830.

Dick, H. J., J. Lin, P. J. Michael, H. Schouten, and J. E. Snow (2002), Ultra-slow-spreading—A new class of ocean ridge, *Eos Trans. AGU*, *83*(47), Fall Meet. Suppl., Abstract T52E-05.

Dick, H. J. B., J. Lin, and H. Schouten (2003), An ultraslow-spreading class of ocean ridge, *Nature*, *426*, 405–412.

Douville, E., J. L. Charlou, E. H. Oelkers, P. Bienvenu, C. F. J. Colon, J. P. Donval, Y. Fouquet, D. Prieur, and P. Appriou (2002), The Rainbow vent fluids (36°14′N, MAR): The influence of ultramafic rocks and phase separation on trace metal content in Mid-Atlantic Ridge hydrothermal fluids, *Chem. Geol.*, *184*, 37–48.

Edmonds, H. N., P. J. Michael, E. T. Baker, D. P. Connelly, J. E. Snow, C. H. Langmuir, H. J. B. Dick, R. Mühe, C. R. German, and D. W. Graham (2003), Discovery of abundant hydrothermal venting on the ultraslow-spreading Gakkel Ridge, Arctic Ocean, *Nature*, *421*, 252–256.

Edwards, M. H., G. J. Kurras, M. Tolstoy, D. R. Bohnenstiehl, B. J. Coakley, and J. R. Cochran (2001), Evidence of recent volcanic activity on the ultraslow-spreading Gakkel ridge, *Nature*, *409*, 808–812.

Fornari, D. J., and R. W. Embley (1995), Tectonic and volcanic controls on hydrothermal processes at the mid-ocean ridge: An overview based on near-bottom and submersible studies, in *Seafloor Hydrothermal Systems: Physical*, *Chemical, Biological, and Geological Interactions*, *Geophys. Monogr. Ser.*, vol. 91, edited by S. Humphris et al., pp. 1–46, AGU, Washington, D. C.

German, C. R., and L. M. Parson (1998), Distributions of hydrothermal activity along the Mid-Atlantic Ridge: Interplay of magmatic and tectonic controls, *Earth. Planet. Sci. Lett.*, *160*, 327–341.

German, C. R., E. T. Baker, C. Mevel, K. Tamaki, and the FUJI Scientific Team (1998a), Hydrothermal activity along the southwest Indian Ridge, *Nature*, *395*, 490–493.

German, C. R., K. J. Richards, M. D. Rudnicki, M. M. Lam, J. L. Charlou, and FLAME Scientific Party (1998b), Topographic control of a dispersing hydrothermal plume, *Earth Planet. Sci. Lett.*, *156*, 267–273.

Grindlay, N. R., J. A. Madsen, C. Rommevaux-Jestin, and J. Sclater (1998), A different pattern of ridge segmentation and mantle Bouguer gravity anomalies along the ultra-slow spreading Southwest Indian Ridge (15°30′E to 25°E), *Earth Planet. Sci. Lett.*, *161*, 243–253.

Jokat, W., O. Ritzmann, M. C. Schmidt-Aursch, S. Drachev, S. Gauger, and J. Snow (2003), Geophysical evidence for reduced melt production on the Arctic ultraslow Gakkel mid-ocean ridge, *Nature*, *423*, 962–965.

Jones, E. P., B. Rudels, and L. G. Anderson (1995), Deep waters of the Arctic Ocean: Origins and circulation, *Deep Sea Res., Part II*, *42*, 737–760.

Kelemen, P. (2003), Igneous crystallization beginning at 20 km beneath the Mid-Atlantic Ridge, 14° to 16°N, *Eos Trans. AGU*, *84*(46), Fall Meet. Suppl., Abstract V22H-03.

Kelley, D. S., et al. (2001), An off-axis hydrothermal vent field near the Mid-Atlantic Ridge at 30°N, *Nature*, *412*, 145–149.

Lavelle, J. W., E. T. Baker, and G. J. Massoth (1998), On the calculation of total heat, salt, and tracer fluxes from ocean hydrothermal events, *Deep Sea Res., Part II*, *45*, 2619–2636.

Lin, J., and J. Phipps Morgan (1992), The spreading rate dependence of three-dimensional mid-ocean ridge gravity structure, *Geophys. Res. Lett.*, *19*, 13–16.

Marsh, A. G., L. S. Mullineaux, C. M. Young, and D. T. Manahan (2001), Larval dispersal potential of the tubeworm Riftia pachyptila at deep-sea hydrothermal vents, *Nature*, *411*, 77–80.

Michael, P. J., et al. (2003), Magmatic and amagmatic seafloor generation at the ultraslow-spreading Gakkel Ridge, Arctic Ocean, *Nature*, *423*, 956–961.

Muller, C., and W. Jokat (2000), Seismic evidence for volcanic activity discovered in central Arctic, *Eos Trans. AGU*, *81*(24), 265–269.

Muller, M. R., T. A. Minshull, and R. S. White (1999), Segmentation and melt supply at the Southwest Indian Ridge, *Geology*, *27*, 867–870.

Münch, U., C. Lalou, P. Halbach, and H. Fujimoto (2001), Relict hydrothermal events along the super-slow Southwest Indian spreading ridge near 63°56′E—Mineralogy, chemistry and chronology of sulfide samples, *Chem. Geol.*, *177*, 341–349.

Murton, B. J., et al. (1994), Direct evidence for the distribution and occurrence of hydrothermal activity between 27°N–30°N on the Mid-Atlantic Ridge, *Earth Planet. Sci. Lett.*, *125*, 119–128.

Nansen, F. (1897), *Farthest North*, Archibold Constable, London.

Nost, O. A., and P. E. Isachsen (2003), The large-scale time-mean ocean circulation in the Nordic Seas and the Arctic Ocean estimated from simplified dynamics, *J. Mar. Res.*, *61*, 175–210.

Reid, I., and H. R. Jackson (1981), Oceanic spreading rate and crustal thickness, *Mar. Geophys. Res.*, *5*, 165–172.

Rudels, B., H. J. Freidrich, and D. Quadfasel (1999), The Arctic circumpolar boundary current, *Deep Sea Res., Part II*, *46*, 1023–1062.

Rudnicki, M. D., and H. Elderfield (1992), Theory applied to the Mid-Atlantic Ridge hydrothermal plumes: The finite difference approach, *J. Volcanol. Geotherm. Res.*, *50*, 161–172.

Salters, V. J. M., and H. J. B. Dick (2002), Mineralogy of the mid-ocean-ridge basalt source from neodymium isotopic composition of abyssal peridotites, *Nature*, *418*, 68–72.

Sauter, D., L. Parson, V. Mendel, C. Rommevaux-Jestin, O. Gomez, A. Briais, C. Mevel, and K. Tamaki (2002), TOBI sidescan sonar imagery of the very slow-spreading Southwest Indian Ridge: Evidence for along-axis magma distribution, *Earth Planet. Sci. Lett.*, *202*, 511–512.

Scheirer, D. S., E. T. Baker, and K. T. M. Johnson (1998), Detection of hydrothermal plumes along the Southeast Indian Ridge near the Amsterdam-St. Paul hotspot, *Geophys. Res. Lett.*, *25*, 97–100.

Snow, J., M. Bock, and H. Feldmann (2002), Evidence for hydrothermal activity, Gakkel Ridge, in *Polarstern ARKTIS XVII/2 Cruise Report: AMORE 2001*, edited by J. Thiede and Shipboard Scientific Party, *Rep. Pol. Mar. Res.*, *421*, 90–93.

Thurnherr, A. M., and K. J. Richards (2001), Hydrography and high-temperature heat flux of the Rainbow hydrothermal site (36°14′N, Mid-Atlantic Ridge), *J. Geophys. Res.*, *106*, 9411–9426.

Thurnherr, A. M., C. R. German, and the AMORES (Theme 1) Science Team (2002), Geochemical and microbial export from the Rainbow vent-site, 36°N Mid-Atlantic Ridge, *Eos Trans. AGU*, *83*(47), Fall Meet. Suppl., Abstract V61B-1362.

Tolstoy, M., D. R. Bohnenstielhl, M. H. Edwards, and G. J. Kurras (2001), Seismic character of volcanic activity at the ultraslow-spreading Gakkel Ridge, *Geology*, *29*, 1139–1142.

Urabe, T., et al. (1995), The effect of magmatic activity on hydrothermal venting along the superfast-spreading East Pacific Rise, *Science*, *269*, 1092–1095.

White, R. S., D. McKenzie, and R. K. O'Nions (1992), Oceanic crustal thickness from seismic measurements and rare earth element inversions, *J. Geophys. Res.*, *97*, 19,683–19,715.

White, R. S., T. A. Minshull, M. J. Bickle, and C. J. Robinson (2001), Melt generation at very slow-spreading oceanic ridges: Constraints from geochemical and geophysical data, *J. Petrol.*, *42*, 1171–1196.

Wilcock, W. S. D., and J. R. Delaney (1996), Mid-ocean ridge sulfide deposits: Evidence for heat extraction from magma chambers or cracking fronts?, *Earth Planet. Sci. Lett.*, *145*, 49–64.